

AD-A104 189

SYSTEMS SCIENCE AND SOFTWARE LA JOLLA CA  
REGIONAL GROUND MOTIONS FROM A ONE MEGATON SURFACE BURST.(U)  
SEP 80 T G BARKER F19628-79-C-  
SSS-R-81-4683 AFGL-TR-80-0377

F/S 8/11

F1962B-79-C-0003

NI

UNCLASSIFIED

138

AEGI-TB-AQ-0377

NI

END

DATE

FILM

8

DTIG

AD A104189

AFGL-TR-80-0377

LEVEL  
12

**REGIONAL GROUND MOTIONS FROM A  
ONE MEGATON SURFACE BURST**

T.G. Barker

Systems, Science and Software  
P.O. Box 1620  
LaJolla, California 92038



**FINAL REPORT  
November 15, 1978 - May 31, 1980**

September 1980

**Approved for Public Release: Distribution Unlimited**

AIR FORCE GEOPHYSICS LABORATORY  
AIR FORCE SYSTEMS COMMAND  
UNITED STATES AIR FORCE  
HANSOM AFB, MASSACHUSETTS 01731

819 14 096

FILE COPY

Qualified requestors may obtain additional copies from the Defense Technical Information Center. All others should apply to the National Technical Information Service.

## UNCLASSIFIED

SECURITY CLASSIFICATION OF THIS PAGE (When Data Entered)

REPORT DOCUMENTATION PAGE		READ INSTRUCTIONS BEFORE COMPLETING FORM
1. REPORT NUMBER AFGL-TR-80-0377	2. GOVT ACCESSION NO. AD-A104189	3. RECIPIENT'S CATALOG NUMBER
4. TITLE (and Subtitle) REGIONAL GROUND MOTIONS FROM A ONE MEGATON SURFACE BURST.	5. TYPE OF REPORT & PERIOD COVERED Final Report 11/15/78 - 5/31/80	
	6. PERFORMING ORG. REPORT NUMBER SSS-R-81-4683 ✓	
7. AUTHOR(s) T. G. Barker	8. CONTRACT OR GRANT NUMBER(s) F19628-79-C-0003 ✓	
9. PERFORMING ORGANIZATION NAME AND ADDRESS Systems, Science and Software P. O. Box 1620 La Jolla, California 92038	10. PROGRAM ELEMENT, PROJECT, TASK AREA & WORK UNIT NUMBERS 61102F 2309G2AD	
11. CONTROLLING OFFICE NAME AND ADDRESS Air Force Geophysics Laboratory Hanscom AFB, Massachusetts 01731 Monitor/Ker C. Thomson/LW	12. REPORT DATE Sept 1980	
14. MONITORING AGENCY NAME & ADDRESS/If different from Controlling Office)	13. NUMBER OF PAGES 78	
16. DISTRIBUTION STATEMENT (of this Report)	15. SECURITY CLASS. (of this report) Unclassified	
Approved for public release; distribution unlimited.	15a. DECLASSIFICATION/DOWNGRADING SCHEDULE	
17. DISTRIBUTION STATEMENT (of the abstract entered in Block 20, if different from Report) <i>Approved for public release; distribution unlimited.</i>		
18. SUPPLEMENTARY NOTES		
19. KEY WORDS (Continue on reverse side if necessary and identify by block number) Surface bursts Regional seismic ground motions Synthetic seismograms Ground motion decay rates		
20. ABSTRACT (Continue on reverse side if necessary and identify by block number) Ground motions from a numerical simulation of a one megaton nuclear surface burst are propagated to regional distances (3.5 to 350 miles) through earth models appropriate to three sites at Minuteman Wings IV, V and VI. Synthetic ground motions and response spectra are examined and compared as functions of range and earth structure. In addition, the ground motions due to the airblast alone were compared with those due to the full surface		

UNCLASSIFIED

SECURITY CLASSIFICATION OF THIS PAGE(When Data Entered)

20. ABSTRACT (continued)

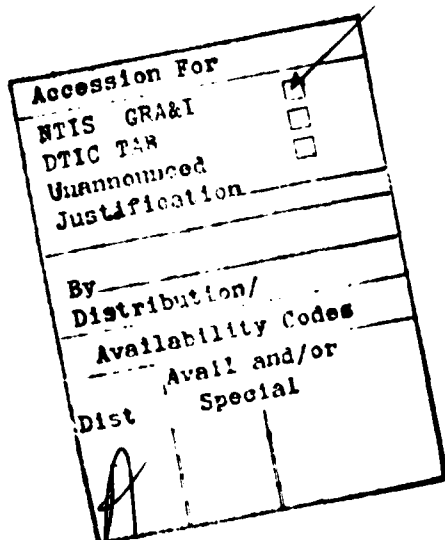
burst simulation and were found to provide a good approximation to the full solution.

UNCLASSIFIED

SECURITY CLASSIFICATION OF THIS PAGE(When Data Entered)

## TABLE OF CONTENTS

<u>Section</u>		<u>Page</u>
I.	INTRODUCTION. . . . .	1
II.	COMPUTATIONAL METHODS . . . . .	3
	2.1 PROPAGATION OF SURFACE WAVES FROM NUMERICAL SIMULATIONS. . . . .	4
	2.2 PROPAGATION OF SURFACE WAVES FROM AN AIRBLAST ON AN ELASTIC HALFSPACE . . . . .	5
III.	EARTH MODELS. . . . .	9
IV.	GROUND MOTION CALCULATIONS. . . . .	19
	4.1 GROUND MOTIONS FROM THE FULL SIMULATION AND THE AIRBLAST OVER AN ELASTIC MEDIUM. . . . .	19
	4.2 THE MIXED PROPAGATION PATH . . . . .	27
	4.3 COMPARISON OF GROUND MOTIONS FOR THREE EARTH STRUCTURES . . . . .	32
	4.4 DEPENDENCE ON Q. . . . .	55
V.	REFERENCES. . . . .	60
APPENDIX A: SYNTHETIC SEISMOGRAMS FROM COMPLEX SOURCE CALCULATIONS. . . . .		62



## LIST OF ILLUSTRATIONS

<u>Figure</u>		<u>Page</u>
1.	The cylindrical surface on which displacement and stresses were monitored in Source 3/5 calculation is shown . . . . .	6
2.	A schematic of the mixed propagation path is shown . . . . .	7
3.	The shear wave ( $\beta$ ) dependence on depth is shown for the three sites. . . . .	10
4.	The shear wave dependence on depth in the upper 10 km is shown for the three sites . . .	11
5.	The anelastic attenuation parameter Q is plotted versus depth . . . . .	14
6.	The short period recording of SALMON at a range of 244 km is shown . . . . .	15
7.	The response spectrum of the portion of the seismogram in Figure 6 between 70 and 84 seconds is shown. . . . .	16
8.	The response spectrum of the portion of the seismogram in Figure 6 between 70 and 98 seconds is shown. . . . .	17
9.	Vertical displacement are shown for the full simulation at W5S3 for five ranges. . . .	20
10.	Vertical displacements for the airblast alone on an elastic medium with mixed propagation path are shown for five ranges . .	21
11a.	Response spectra for the full simulation is compared with the airblast alone solutions for the W5S3 earth model at $r = 5.63$ km. . . . .	22
11b.	Response spectra for the full simulation is compared with the airblast alone solutions for the W5S3 earth model at $r = 16.1$ km. . . . .	23
11c.	Response spectra for the full simulation is compared with the airblast alone solutions for the W5S3 earth model at $r = 56.3$ km. . . . .	24

LIST OF ILLUSTRATIONS (continued)

<u>Figure</u>		<u>Page</u>
11d.	Response spectra for the full simulation is compared with the airblast alone solutions for the W5S3 earth model at $r = 161.0$ km . . . . .	25
11e.	Response spectra for the full simulation is compared with the airblast alone solutions for the W5S3 earth model at $r = 563.0$ km . . . . .	26
12a.	Peak values in PRD are plotted versus range for the full simulation and the airblast/elastic case. . . . .	29
12b.	Peak values of PSRV are plotted versus range for the full simulation and the airblast/elastic case. . . . .	30
12c.	Peak values of PSAA are plotted versus range for the full simulation and the airblast/elastic case. . . . .	31
13.	Synthetic displacement seismograms for the airblast/elastic case with a single propagation path are shown . . . . .	33
14a.	Response spectra for the airblast on an elastic medium for the mixed path and for the single path are shown; $r = 5.63$ km . . . .	34
14b.	Response spectra for the airblast on an elastic medium for the mixed path and for the single path are shown; $r = 16.1$ km . . . .	35
14c.	Response spectra for the airblast on an elastic medium for the mixed path and for the single path are shown; $r = 56.3$ km . . . .	36
14d.	Response spectra for the airblast on an elastic medium for the mixed path and for the single path are shown; $r = 161.0$ km. . . .	37
14e.	Response spectra for the airblast on an elastic medium for the mixed path and for the single path are shown; $r = 563.0$ km. . . .	38

**LIST OF ILLUSTRATIONS (continued)**

<u>Figure</u>		<u>Page</u>
15a.	Peak values of PRD are plotted versus range for the airblast/elastic source with a single and a mixed propagation path . . . . .	39
15b.	Peak values of PSRV are plotted versus range for the airblast/elastic source with a single and a mixed propagation path . . . . .	40
15c.	Peak values of PSAA are plotted versus range for the airblast/elastic source with a single and a mixed propagation path . . . . .	41
16.	Synthetic displacement seismograms at W5S3 for the airblast/elastic case with a single propagation path are shown. . . . .	43
17.	Synthetic displacement seismograms at W4S8 for the airblast/elastic case with a single propagation path are shown. . . . .	44
18.	Synthetic displacement seismograms at W6S1 for the airblast/elastic case with a single propagation path are shown. . . . .	45
19a.	Response spectra for the airblast/elastic case with a single propagation path are shown for the three sites at $r = 5.63$ km . . .	47
19b.	Response spectra for the airblast/elastic case with a single propagation path are shown for the three sites at $r = 16.1$ km . . .	48
19c.	Response spectra for the airblast/elastic case with a single propagation path are shown for the three sites at $r = 56.3$ km . . .	49
19d.	Response spectra for the airblast/elastic case with a single propagation path are shown for the three sites at $r = 161.0$ km. . .	50
19e.	Response spectra for the airblast/elastic case with a single propagation path are shown for the three sites at $r = 563.0$ km. . .	51

LIST OF ILLUSTRATIONS (continued)

<u>Figure</u>		<u>Page</u>
20a.	Peak values of PRD are plotted versus range for W5S3, W4S8 and W6S1. . . . .	52
20b.	Peak values of PSRV are plotted versus range for W5S3, W4S8 and W6S1. . . . .	53
20c.	Peak values of PSAA are plotted versus range for W5S3, W4S8 and W6S1. . . . .	54
21a.	Peak values of PRD are plotted for W5S3 using the Q model in Figure 5 and using that model with all values of Q divided by two . . . . .	57
21b.	Peak values of PSRV are plotted for W5S3 using the Q model in Figure 5 and using that model with all values of Q divided by two . . . . .	58
21c.	Peak values of PSAA are plotted for W5S3 using the Q model in Figure 5 and using that model with all values of Q divided by two . . . . .	59

## I. INTRODUCTION

In the first report for this contract, Rimer, et al. (1980) described the calculations which carried the Source 3/5 ground coupling calculation for a one megaton near surface nuclear explosion into the elastic regime. In this report we propagate this elastic wavefield into the far field and compare these results with the ground motion induced by only the airblast part of the explosion.

Synthetic seismograms and response spectra were calculated for ranges varying from 3.5 miles to 350 miles (5.63 km to 563 km) for three sites within Minuteman Wings IV, V and VI. The results were examined for their dependencies on

- range
- crustal structure
- source (full explosion simulation on a non-linear soil model versus the airblast alone on an elastic medium).

The ranges (3.5, 10, 35, 100 and 350 miles) and sites were suggested by TRW engineers and approved by Weidlinger Associates. The earth models were constructed using data from TRW and from the literature for Site 3 at Wing V, Site 1 at Wing VI and Site 8 at Wing IV.

Peaks in the computed pseudo relative velocity (PSRV) spectra fall off from values between 20 cm/sec and 100 cm/sec at 5.63 km to values between  $10^{-3}$  cm/sec and  $10^{-2}$  cm/sec at 563 km, depending on the earth model. The rate of decay with range is about  $r^{-2}$  to  $r^{-2.5}$ . At 5.63 km, the pseudo absolute accelerations (PSAA) peak at 0.5 g to 5.0 g and decay at a rate of about  $r^{-3}$  to  $10^{-5}$  g to  $10^{-4}$  g at 563 km. The peaks occur at periods near 1 second for the closest range, near 3 seconds at intermediate distances and near 10 seconds at the farthest position.

Except at the closest position, the peak amplitudes in PSRV and PSAA for the full simulation were within a factor of two of those for the airblast alone. The periods of maximum PSRV and PSAA agreed closely for both sources. The difference in close are at short periods and are most likely due to the difference in response of the elastic solid for the airblast alone and the nonlinear soil response in the full simulation. As did Murphy and Bennett (1979), we conclude that the airblast alone on an elastic halfspace provides an inexpensive yet accurate way of estimating far field ground motions from a surface burst.

The report is divided into three remaining sections. Section II describes the mathematical and numerical methods used for calculating far field ground motions. The earth models (elastic and anelastic crustal models) are discussed in the third section. The synthetic seismograms and response spectra are shown and compared in the final section.

## II. COMPUTATIONAL METHODS

The purpose of this work is to estimate ground motions from an explosion on the earth's surface. To do this requires an earth model and a method for computing displacements for that model. This necessarily involves assumptions that make the calculations tractable without sacrificing features that affect the observed displacements. Our primary assumptions are:

1. that the earth can be modeled as a plane-layered halfspace,
2. that the dominant ground motions are surface wave motions; and
3. that we can restrict our attention to periods longer than one second.

Within a geologic province, the plane-layered earth assumption is fairly good at long periods. For short periods, however, dipping and curving interfaces and other irregularities are important. Since we have no accurate knowledge of these deviations from plane layers (or inexpensive means for including their effects), it is unrealistic to compute motions for short periods. We have chosen one second as a cutoff.

Numerous observations and calculations have shown that for these periods the dominant ground motions at more than a few kilometers from a surface source are surface waves. That is not to say that the body waves would not be evident, but that they may be safely ignored in estimating peak ground motions. Our calculations then are for surface waves only, but will include higher modes. The number of modes (fundamental plus five overtones) was chosen to represent the entire surface wave solution for periods greater than one second. In the next section, response spectra will be shown for shorter periods because the calculation for individual modes was computed to frequencies high enough to prevent aliasing.

Surface waves are the part of the solution obtained by evaluation of residues. That is, when evaluating the wave number integrals obtained by spatial and temporal Fourier transforms, one finds only the contribution due to poles in the complex plane. This is not the complete solution as branch line integrals contribute also. The branch line integrals are responsible for the body waves but also cancel an acausal long period contribution from the residues. Swanger and Boore (1978) and Herrmann (1977) show that at smaller ranges the acausal surface wave signal can be seen but is small and has little effect on peak motions. At large ranges, the acausal signal is insignificant. Because of this acausal residue solution in our surface wave calculations, the time series (seismograms) are shifted by 40 seconds in the displays in Section IV.

In the remainder of this section we describe the methods for computing multimode surface waves from both the Source 3/5 simulation and the airblast alone.

## 2.1 PROPAGATION OF SURFACE WAVES FROM NUMERICAL SIMULATIONS

The details for propagating the elastic wavefield from a surface in a numerical grid is described in detail in Bache, et al. (1980). An excerpt from their work is included in Appendix A. The method involves spatial and temporal convolutions of monitored displacements and stresses with a particular set of Green's functions. These Green's functions are the displacements and stresses due to forces applied at the point to which the wavefield is to be propagated. We compute only the surface wave contribution to the Green's functions since we have chosen to use only these types of waves in our analysis.

The explosion simulation in Rimer, et al. (1980) was done in a material with constant elastic properties. The surface on which the wave motions were monitored extended to

a depth of 578 meters (Figure 1). Since the crustal models for the sites of interest do not have a single constant layer in the upper 578 meters, a means for making the transition from the near-source region to the remainder of the propagation path is needed. Alewine (1974) gives a transmission coefficient  $T(\omega)$  across this boundary

$$T(\omega) = \left( \frac{C_S A_{R_S}}{C_R A_{R_R}} \right)^{1/2},$$

where  $C_S$  and  $C_R$  are the phase velocities in the source and receiver parts of the path, and  $A_{R_S}$  and  $A_{R_R}$  are the source-depth independent part of the surface wave excitation (Figure 2). Following Bache, Rodi and Harkrider (1978), the solution for the mixed path, for example  $G_r^R$  from Equation (A.11), is

$$G_r^R = i\pi A_{R_R} \epsilon_0 X(z) J_1(kr) H_1^{(2)} \left( \frac{\omega R_S}{C_S} + \frac{\omega R_R}{C_R} \right) e^{-(\gamma_{R_R}^R + \gamma_{S_S}^R)}.$$

For calculations involving the mixed path, we used a source region  $R_S$  which was 25 percent of the total path at the two close ranges (5.63 and 16.1 km) and was 25 km for the farther ranges (56.3, 161 and 563 km).

## 2.2 PROPAGATION OF SURFACE WAVES FROM AN AIRBLAST ON AN ELASTIC HALFSPACE

An aspect of this study is to assess the degree to which the ground motions from the full nonlinear simulation of a large nuclear explosion can be approximated by those from the airblast alone acting on a linear elastic halfspace. In this subsection we show how surface waves due to the airblast overpressure of Needham, *et al.* (1975) (used in the Source 3/5 calculation) are computed.

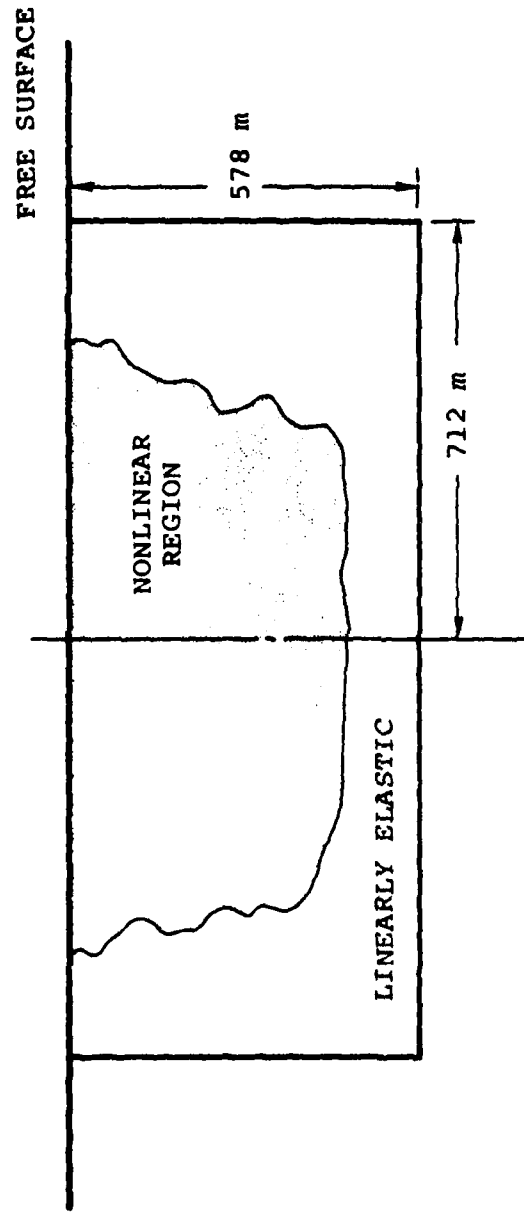


Figure 1. The cylindrical surface on which displacement and stresses were monitored in Source 3/5 calculation is shown.

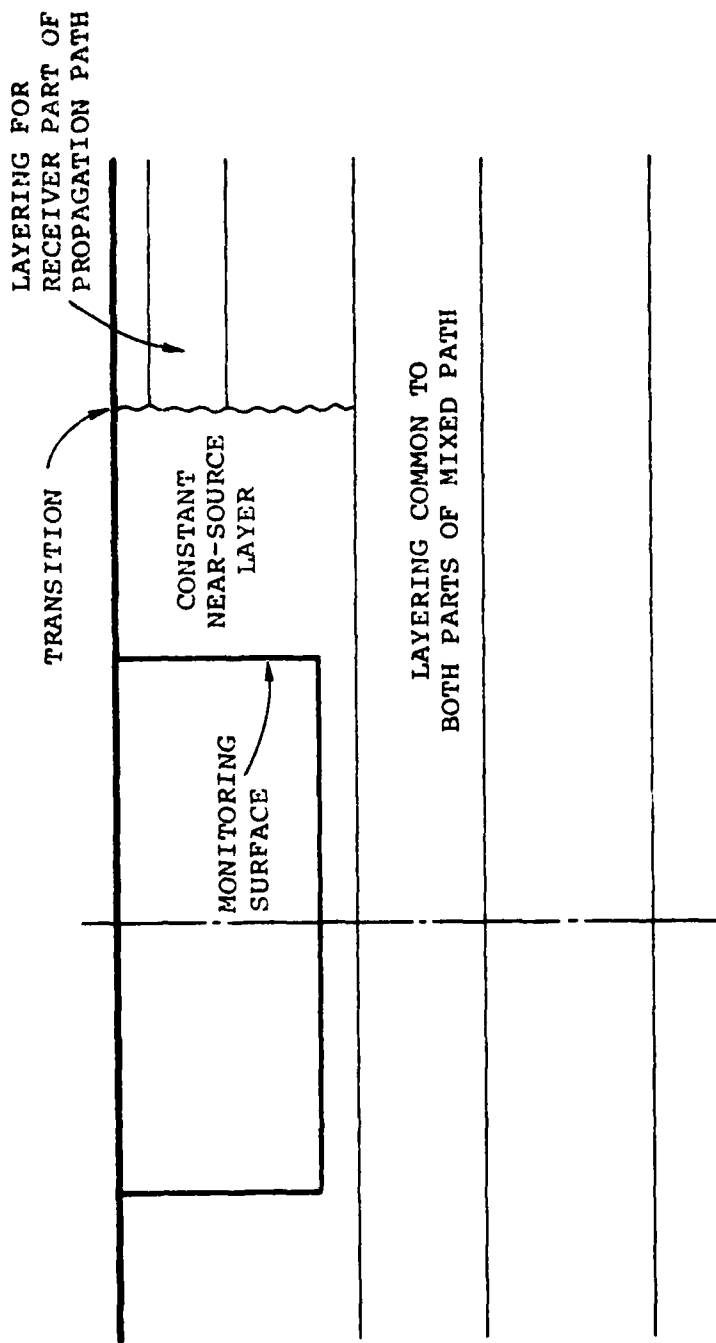


Figure 2. A schematic of the mixed propagation path is shown.

We use the results of Bache, Masso and Mason (1977). Denote the airblast overpressure by  $P(r,t)$ , and define

$$P(\omega) = \int_0^\infty dt e^{-i\omega t} \int_0^\infty P(r,t) J_0(kr) r dr .$$

The vertical surface wave displacement is then

$$w = -i\pi A_R H_0^{(2)}(kR) \hat{P}(\omega)$$

and the radial displacement is

$$u = \epsilon_0 \frac{H_1^{(2)}(kR)}{H_0^{(2)}(kR)} w .$$

Anelastic attenuation and mixed path effects are included as in Section 2.1.

### III. EARTH MODELS

In this section we describe the specific crustal models used in our calculations. The models are appropriate to three locations:

1. Wing V, Site 3 (referred to as W5S3)
2. Wing IV, Site 8 (W4S8), and
3. Wing VI, Site 1 (W6S1).

The upper crust at the three sites were provided by TRW engineers. The lower crust beneath Wing V is the Northern Colorado Plateau model of Keller, et al. (1976). The North Dakota crust at Wing VI was based on refraction surveys in southwestern Manitoba and southeastern Saskatchewan by Green, et al. (1980). The refraction studies by Healey and Warren (1969) in northwestern Missouri provided a model of the crust at Wing IV. The shear wave dependence on depth for the crust is illustrated in Figure 3 and in Figure 4, where the upper 10 km is emphasized. All elastic properties are listed in Table 1.

Geophysical studies generally yield good estimates for elastic properties of the crust. Studies to determine the anelastic attenuation factors  $\gamma$  (and ultimately  $Q$ ) have met with mixed success. At long periods the results seem fairly good. At periods less than 10 seconds, however, the results are scattered with a corresponding lack of confidence in their validity. The primary difficulty is that in order to isolate the effects of anelastic attenuation it is necessary to have a thorough understanding of the elastic properties and an ability to remove their effects. The elastic effects are usually accounted for by using plane-layered models, so that  $\gamma$  and  $Q$  end up accounting not only for anelastic absorption

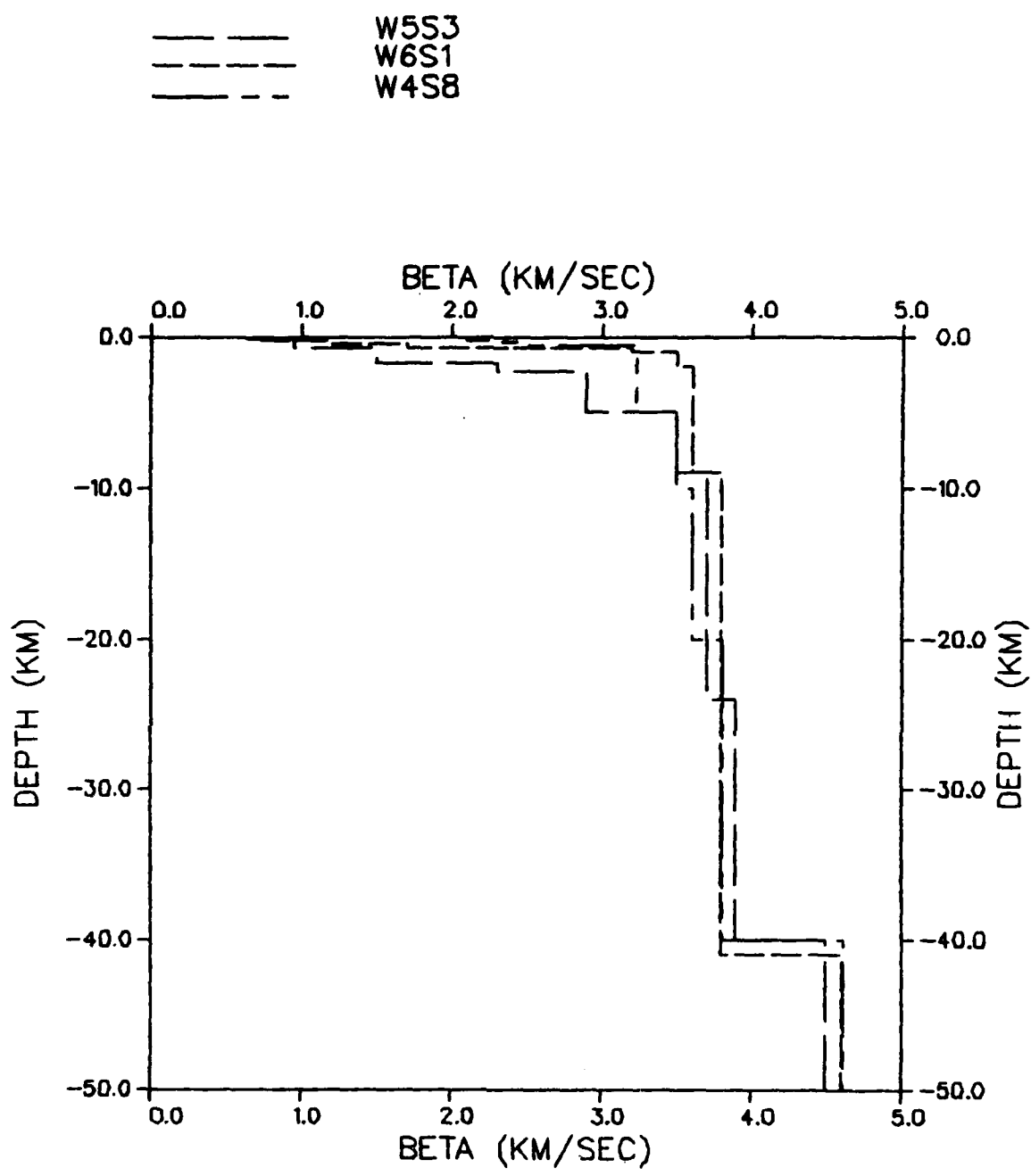


Figure 3. The shear wave ( $\beta$ ) dependence on depth is shown for the three sites.

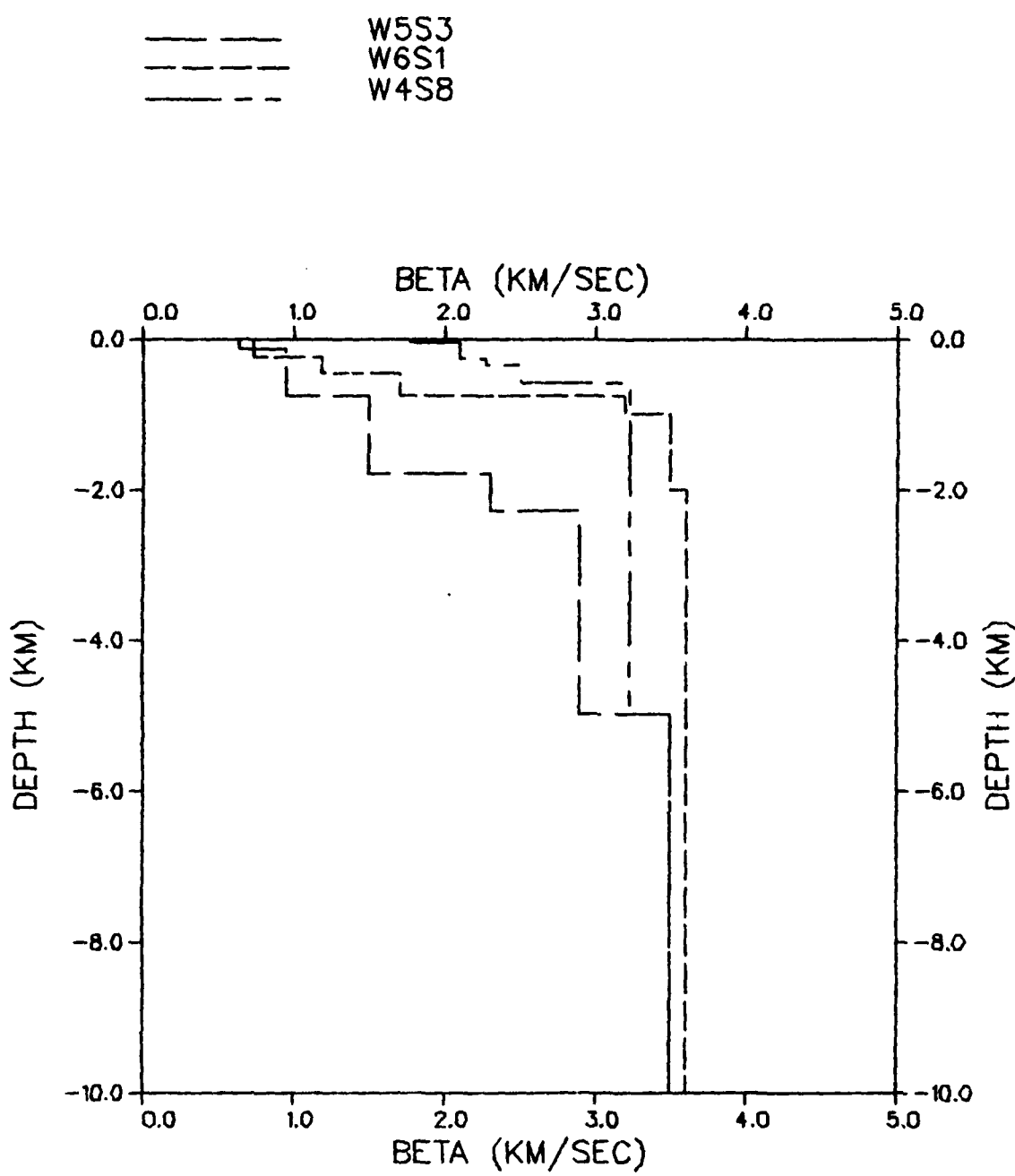


Figure 4. The shear wave dependence on depth in the upper 10 km is shown for the three sites.

TABLE 1  
EARTH MODELS

Layer Thickness (km)	$\alpha$ (km/sec)	$\beta$ (km/sec)	$\rho$ (gm/cm <sup>3</sup> )	$Q_\beta$
<u>W5S3</u>				
0.13	1.10	0.64	1.80	20
0.63	2.30	0.95	2.30	20
1.04	3.20	1.50	2.60	35
0.50	4.40	2.30	2.65	50
2.70	5.50	2.90	2.70	250
4.00	6.10	3.50	2.75	400
15.00	6.40	3.70	2.80	1200
16.00	6.80	3.90	2.90	2000
1.00	7.80	4.50	3.20	2000
<u>W6S1</u>				
0.24	1.70	0.74	2.40	20
0.22	2.20	1.19	2.60	20
0.30	3.20	1.70	2.70	35
0.24	5.50	3.20	2.70	225
1.00	6.00	3.50	2.70	300
7.00	6.20	3.60	2.80	400
16.00	6.60	3.80	2.90	1200
16.00	6.60	3.80	2.90	1800
1.00	8.00	4.60	3.20	2000
<u>W4S8</u>				
0.053	3.51	1.77	2.50	20
0.221	3.93	2.10	2.67	20
0.086	4.25	2.27	2.67	20
0.240	4.68	2.50	2.67	20
2.000	5.60	3.23	2.68	50
2.400	5.60	3.23	2.68	250
5.000	6.10	3.50	2.69	300
10.000	6.20	3.60	2.70	1200
20.000	6.60	3.81	2.90	1800
1.000	8.00	4.62	3.30	2000

but also for elastic scattering and curving or dipping interfaces. Because our choice of Q model strongly affects seismic amplitudes it is important that we make the best choice possible.

Although this is still a relatively unexplored field, especially at short periods, we can use the results of Bache, Swanger and Shkoller (1980). In their work, they compared regional synthetic and observed surface wave recordings for periods around one second. They deduce a Q model based on matching of frequency content, peak amplitude, and signal duration. The Q models used in our calculations are based on techniques developed in their work. Figure 5 shows the Q models.

A shortcoming of the synthetic seismograms computed by Bache, Swanger and Shkoller (1980) is that the signal duration is shorter than the observations. Presumably the seismograms we have computed for this project suffer in the same way. However, we can show that this has little affect on the resulting response spectra. Consider the seismogram shown in Figure 6 which is a recording of the SALMON explosion at a range of 244 km. This recording was made by a short period instrument whose response peaks at 3 Hz which greatly attenuates the longer period dominant surface waves and enhances the body waves. The surface wave portion of this record begins roughly with signals arriving at an apparent velocity of 3.5 km/sec (70 seconds). Synthetic surface wave seismograms show ground motion dominated by waves traveling with speeds in the range 3.5 to 2.9 km/sec (84 seconds). The observed ground motions last much longer. Response spectra of the time interval from 70 to 84 seconds and for a section twice as long from 70 to 98 seconds are shown in Figures 7 and 8. Clearly the two spectra are very close except at the periods longer than the sample intervals. Thus the weakness that calculated seismograms using the Q model of Bache, Swanger and Shkoller

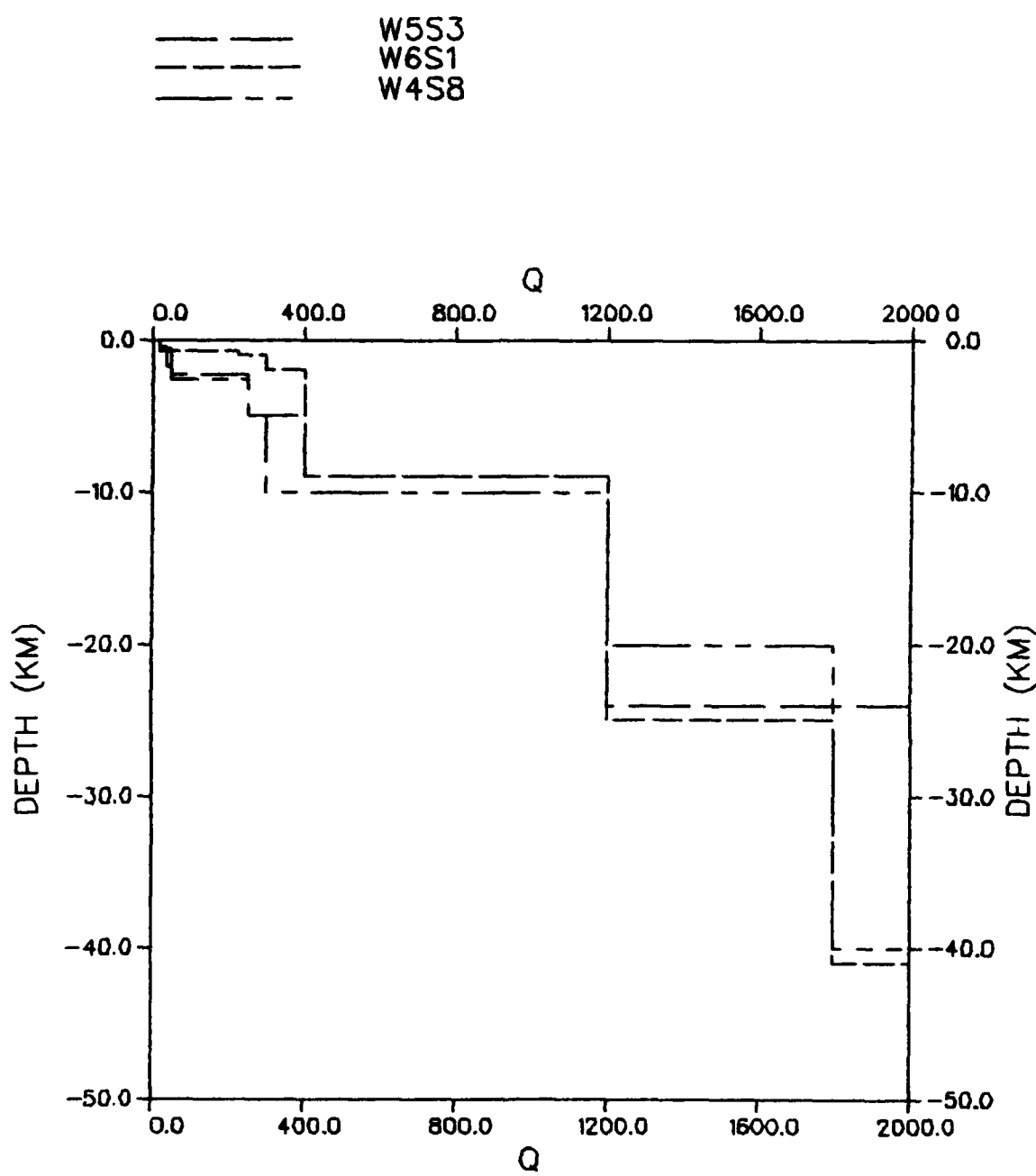


Figure 5. The anelastic attenuation parameter Q is plotted versus depth.

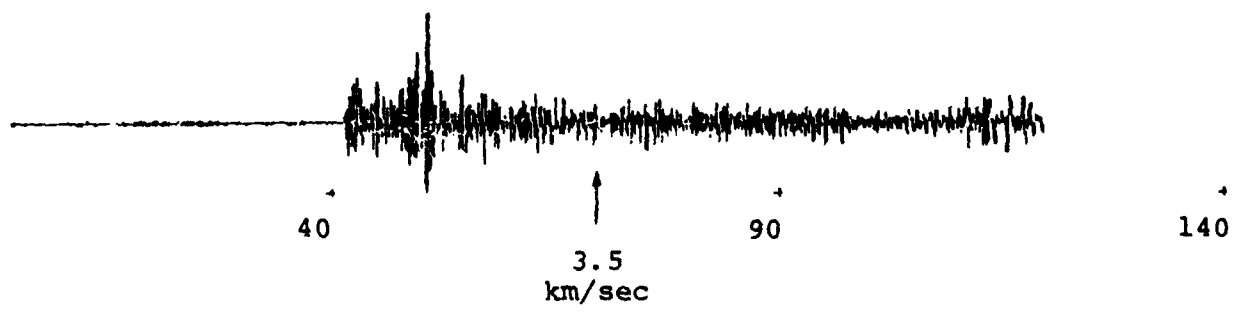


Figure 6. The short period recording of SALMON at a range of 244 km is shown.

SALMON 30117      FROM 3.5 TO 2.9 H/S

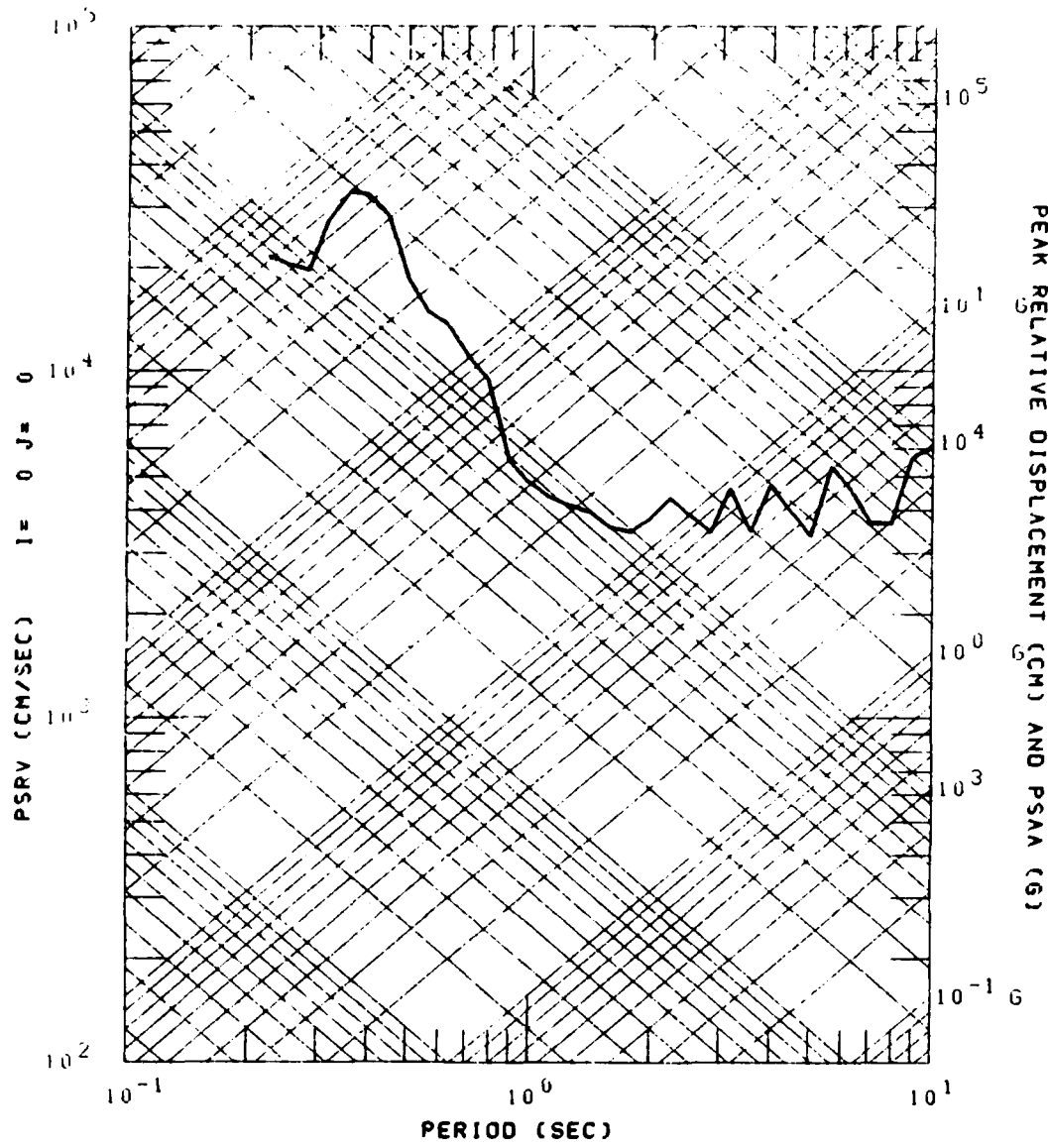


Figure 7. The response spectrum of the portion of the seismogram in Figure 6 between 70 and 84 seconds is shown.

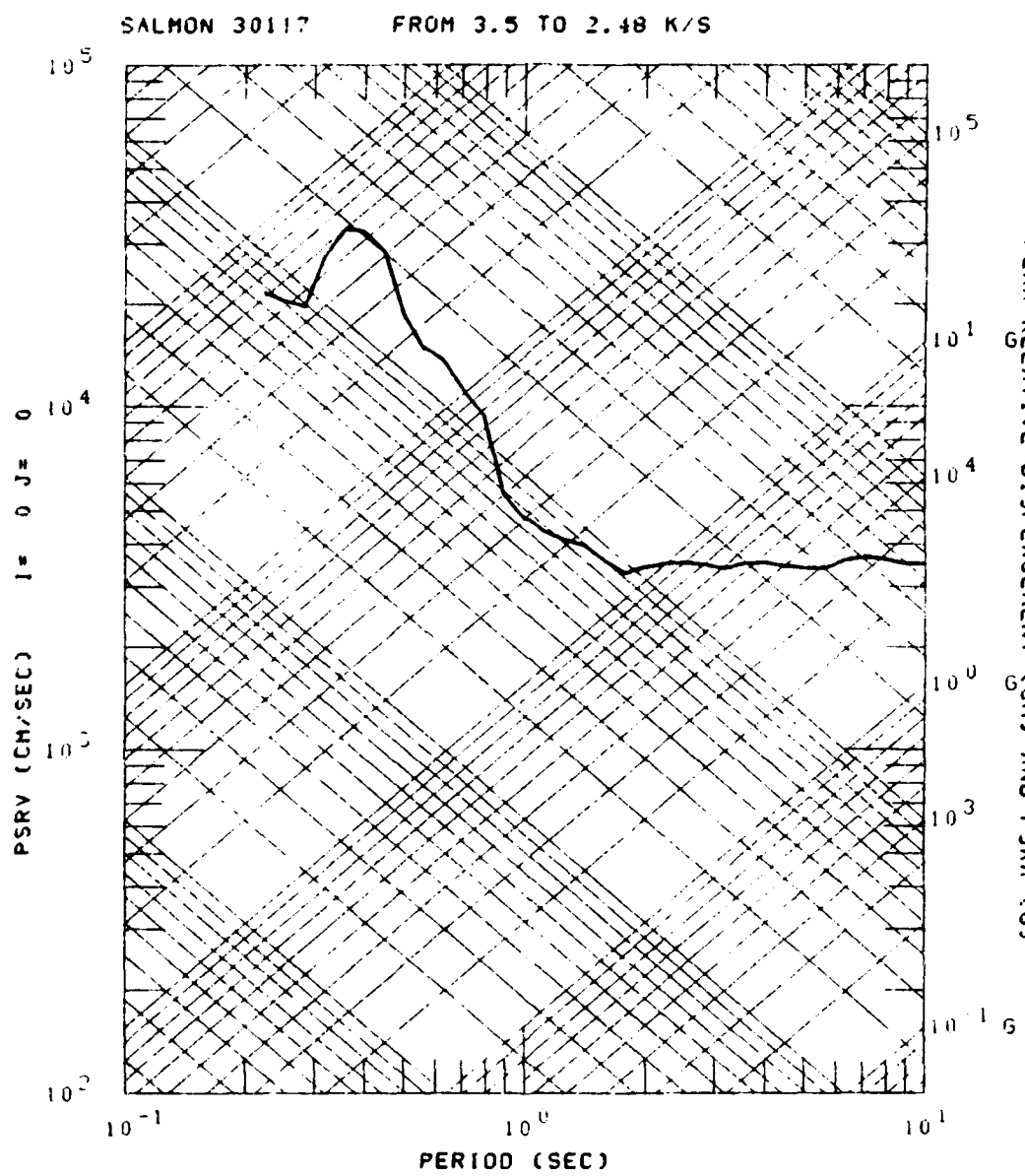


Figure 8. The response spectrum of the portion of the seismogram in Figure 6 between 70 and 98 seconds is shown.

(1980) do not match the observed signal durations does not affect the peak period and amplitude of the corresponding response spectra.

The relative values of Q in these models are more closely constrained than the absolute values. To estimate the effect of having chosen our values of Q to be a factor of two too large (an extreme), we have computed seismograms using our Q model scaled by one-half.

#### IV. GROUND MOTION CALCULATIONS

The objective of the calculations described in this section is to determine the differences in ground motion due to

- the full simulation of the explosion versus the airblast on an elastic medium,
- the distance from ground zero, and
- the crustal models that typify the Minuteman wings chosen for this study.

We begin our discussion with an analysis of the ground motion from the full surface burst simulation versus that produced by only the airblast.

##### 4.1 GROUND MOTIONS FROM THE FULL SIMULATION AND THE AIRBLAST OVER AN ELASTIC MEDIUM

This comparison is performed on the W5S3 structure. Figures 9 and 10 show the calculated vertical displacements at the five ranges for the two sources. Figures 11a through 11e compare the corresponding response spectra. The airblast alone calculation was done with exactly the same mixed propagation path and overpressure function (from Needham, *et al.*, 1976) that were used for the full simulation. The differences in response are due only to the source (airblast alone versus airblast plus radiation effects) and to the soil response (elastic versus nonlinear near source soil models).

The peak displacements from the seismograms for the full simulation range from a few centimeters at  $r = 5.63$  km to a few microns at  $r = 563$  km. Those from the airblast/elastic source are the same at  $r = 56.3$  and two to four times as great at the other ranges. The shapes of the seismograms are basically very similar but have many differences in detail.

Murphy and Bennett (1979) made similar comparisons between the vertical displacements at 1800 meters from another

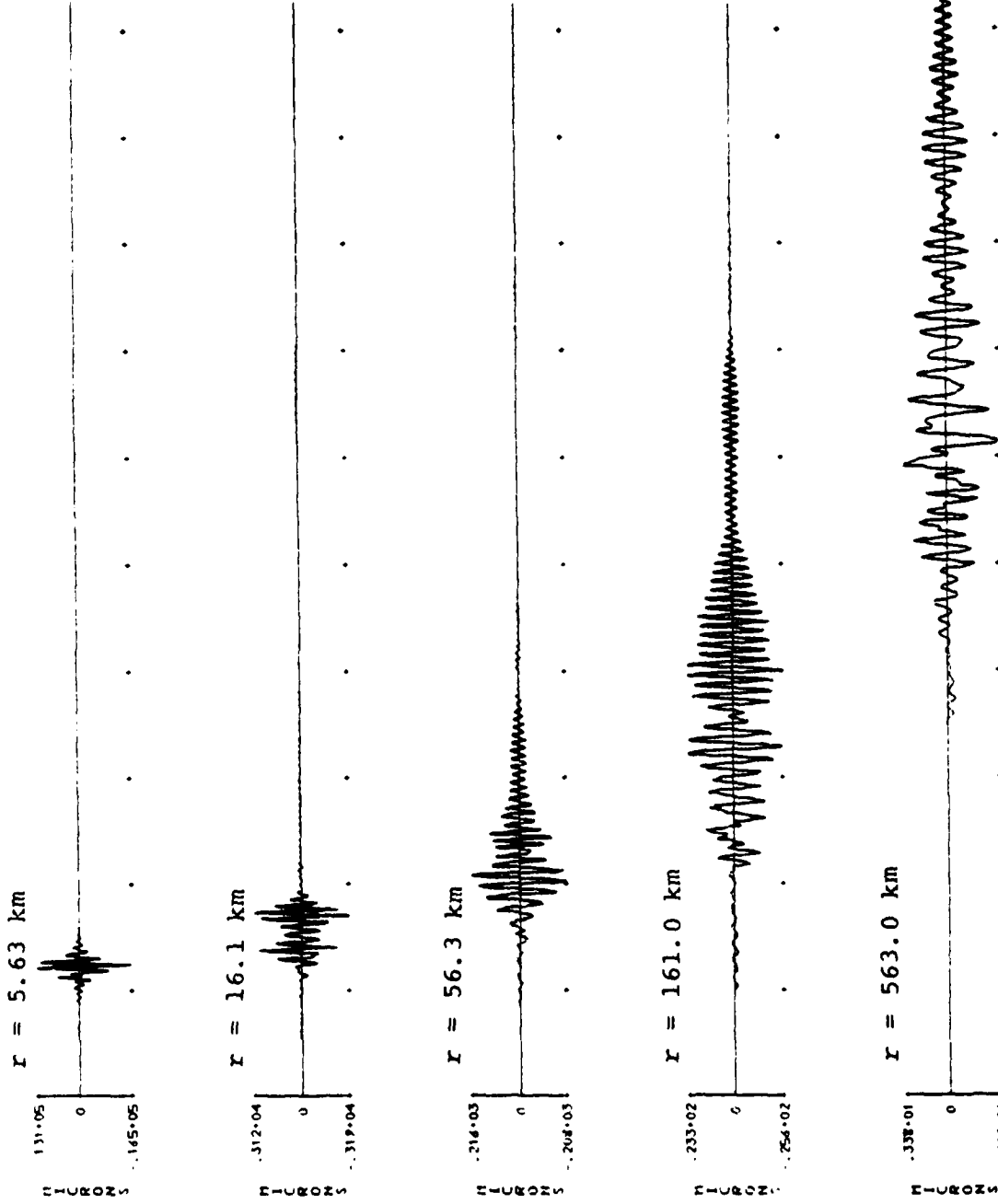
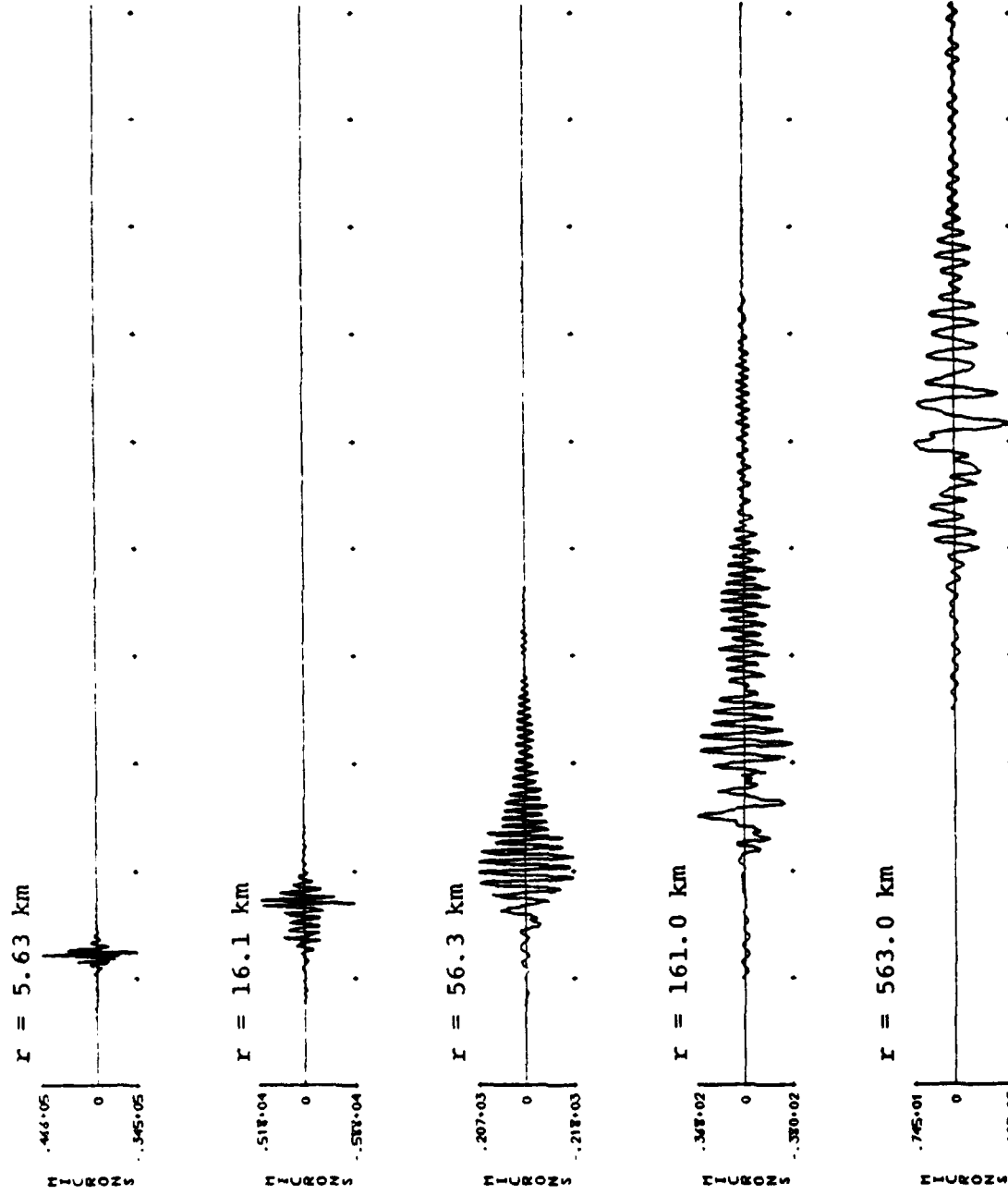


Figure 9. Vertical displacement (microns) are shown for the full simulation at W5S3 for five ranges. Tick marks are at 40 second intervals, beginning at -40 seconds.



**Figure 10.** Vertical displacements (microns) for the airblast alone on an elastic medium with mixed propagation path are shown for five ranges. Tick marks are at 40 second intervals, beginning at -40 seconds.

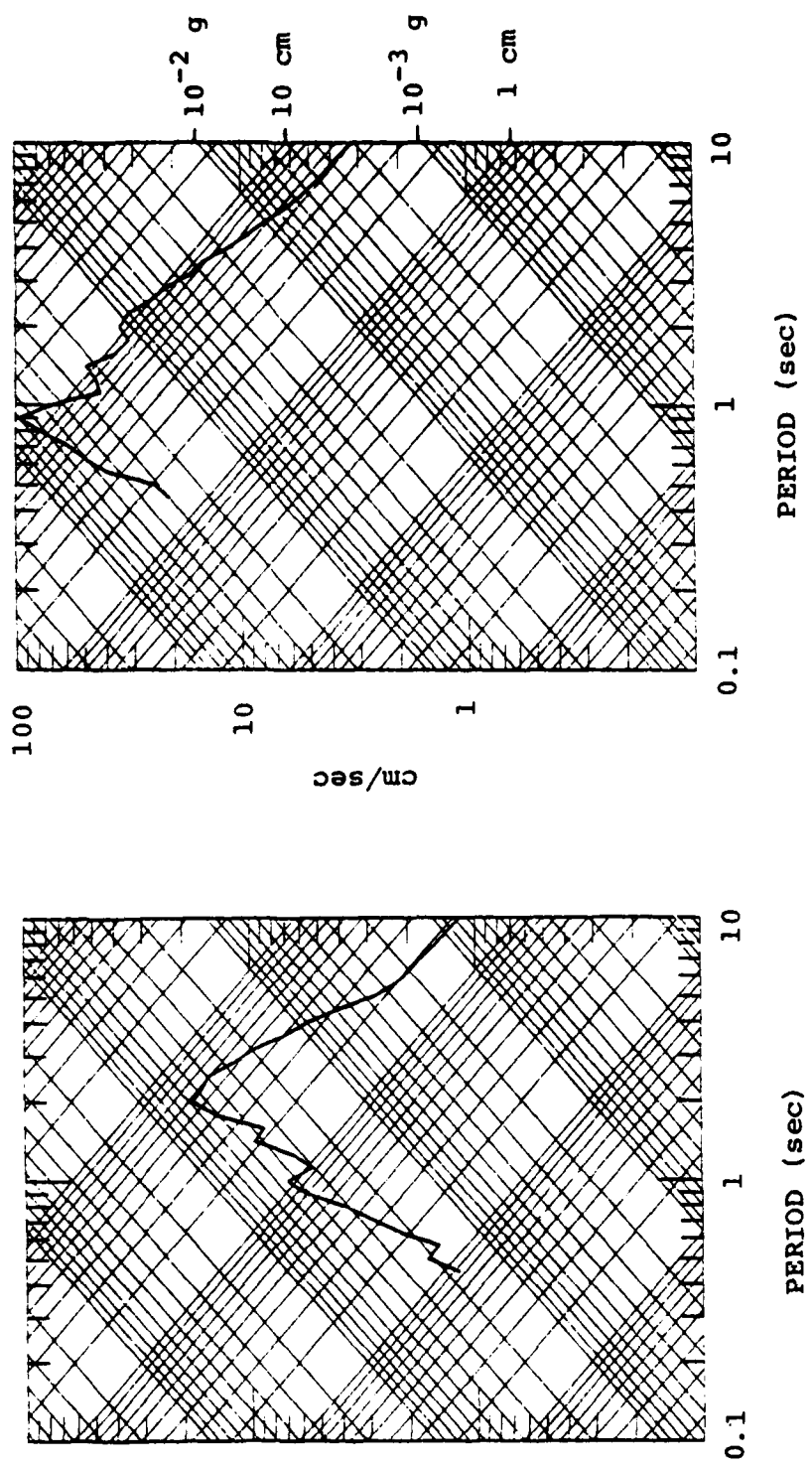


Figure 11a. Response spectra for the full simulation (left) is compared with the airblast alone solutions for the W5S3 earth model at  $r = 5.63$  km.

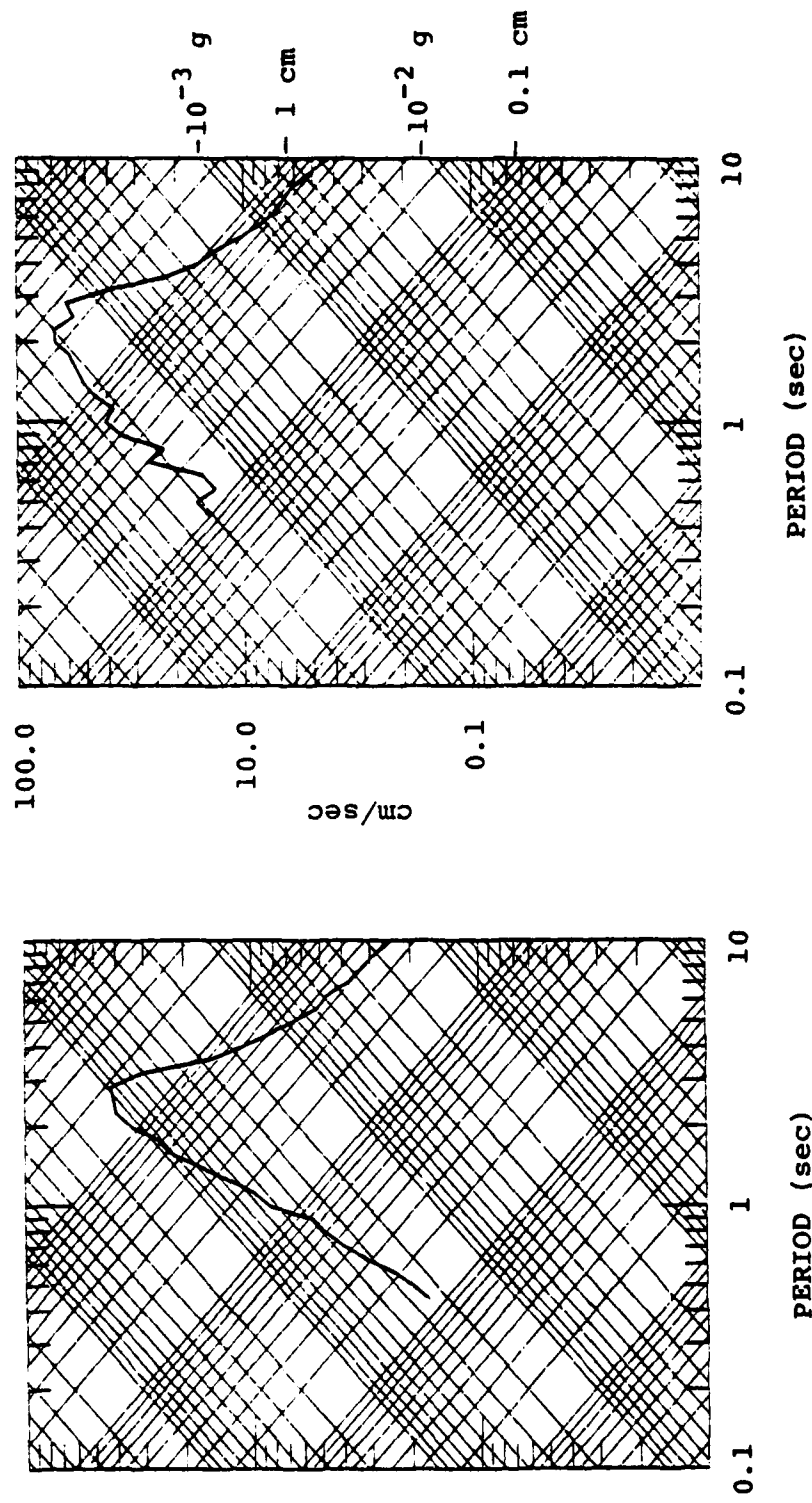
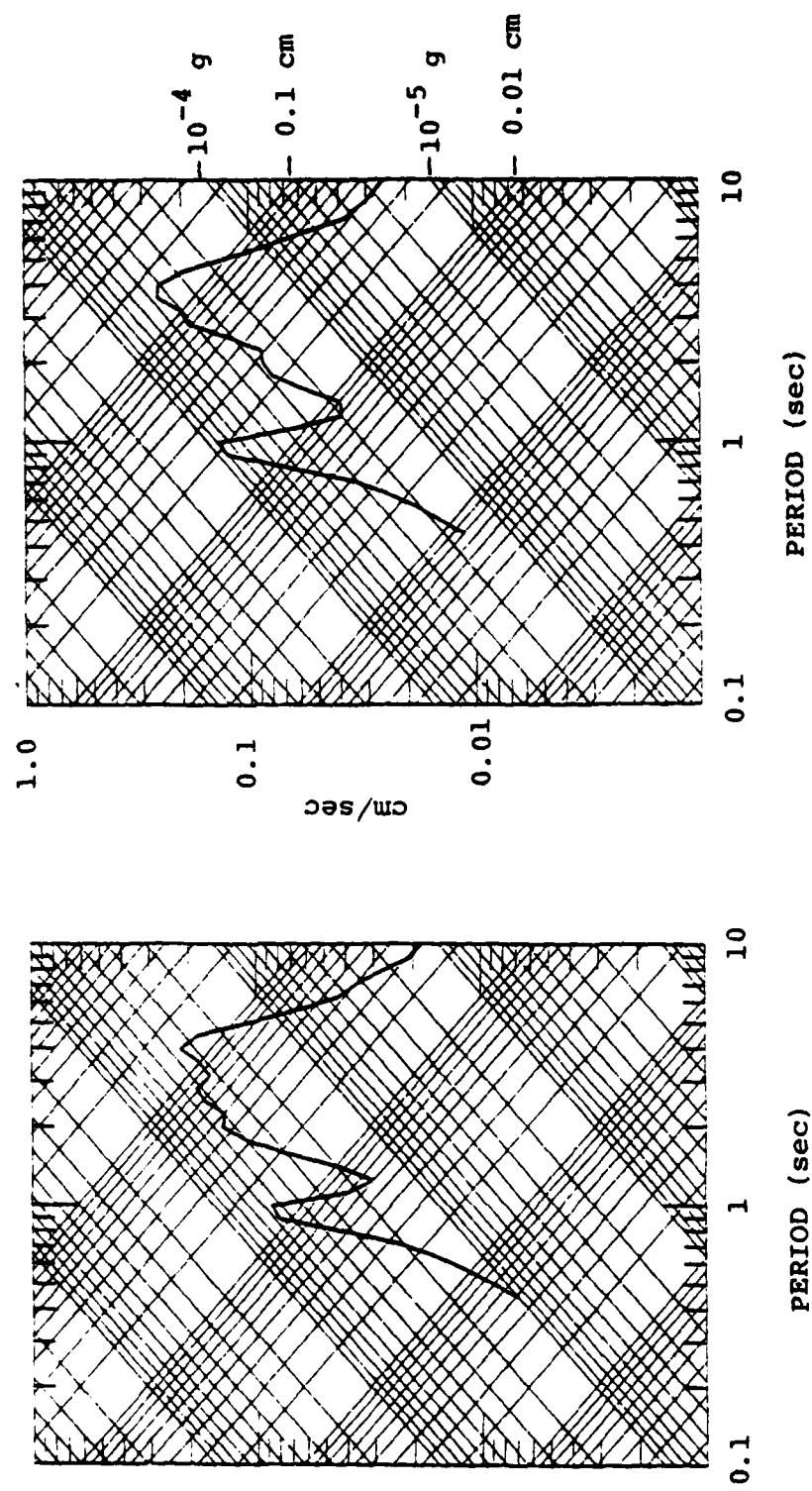


Figure 11b. Response spectra for the full simulation (left) is compared with the airblast alone solutions for the W53 earth model at  $r = 16.1$  km.



**Figure 11c.** Response spectra for the full simulation (left) is compared with the airblast alone solutions for the W5S3 earth model at  $r = 56.3$  km.

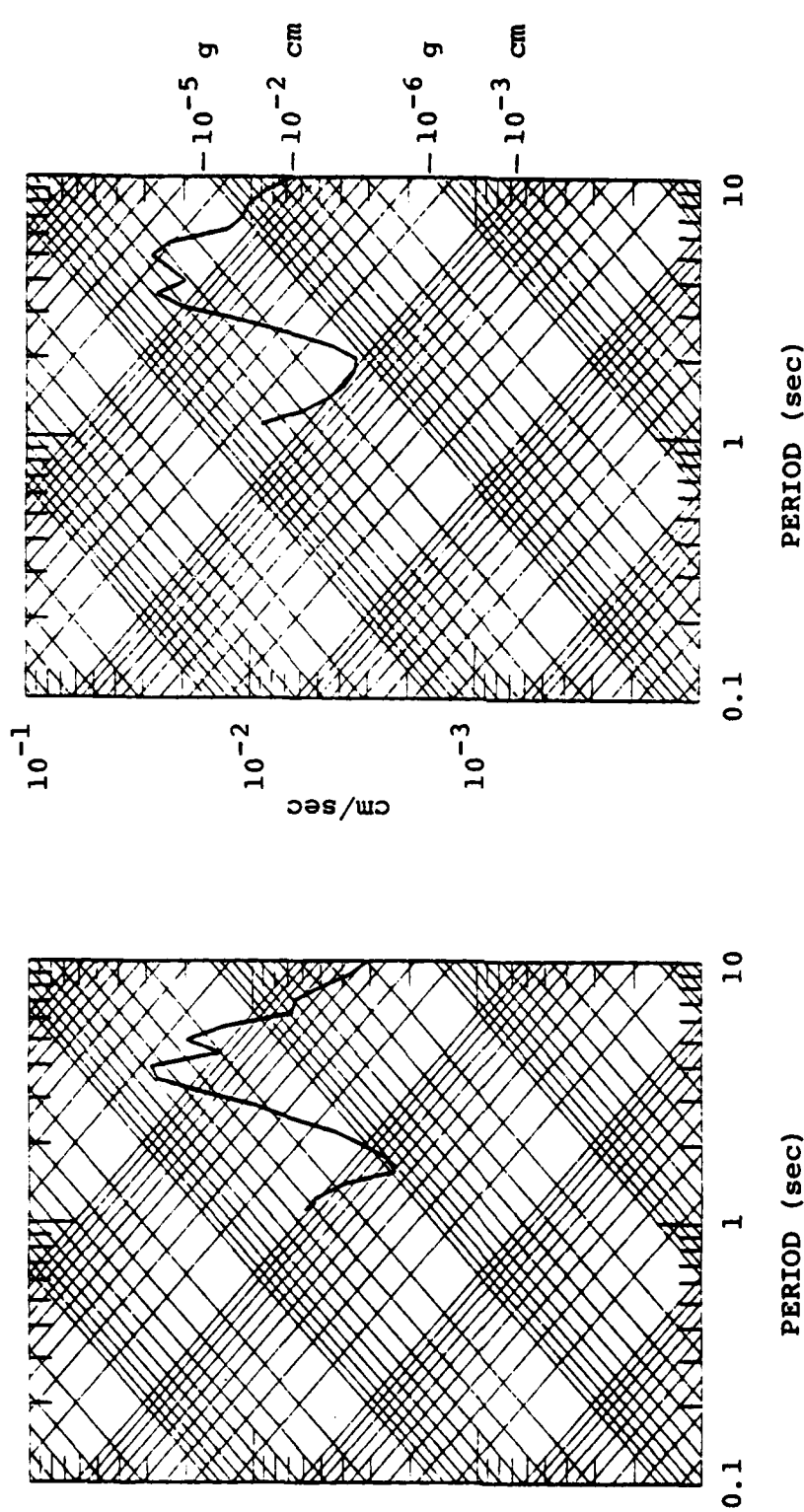


Figure 11d. Response spectra for the full simulation (left) is compared with the airblast alone solutions for the W5S3 earth model at  $r = 161.0$  km.

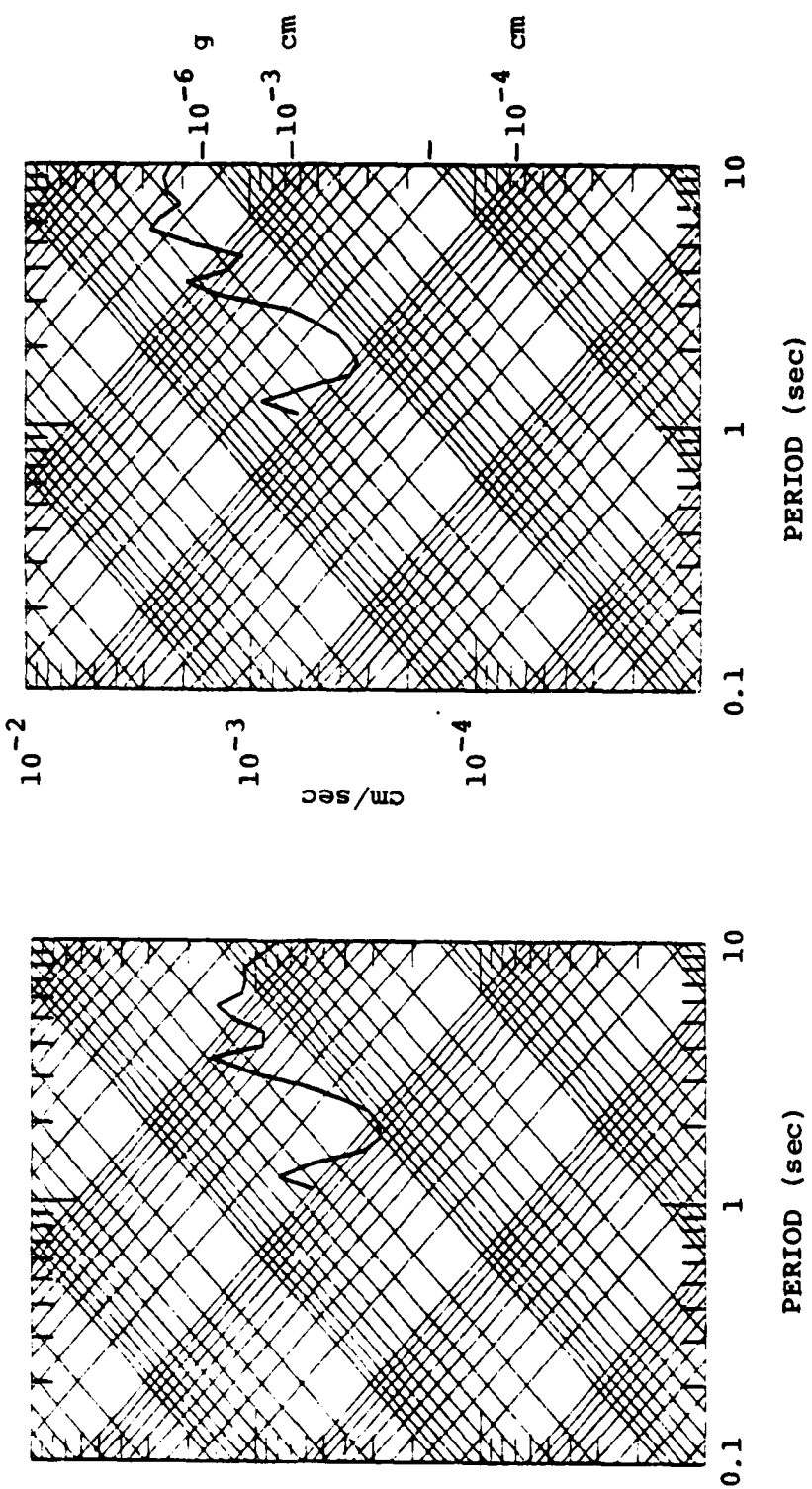


Figure 11e. Response spectra for the full simulation (left) is compared with the airblast alone solutions for the W5S3 earth model at  $r = 563.0$  km.

nonlinear finite difference simulation of the airblast loading (by Sandler, 1978) and from an airblast over an elastic half-space. They found that the general character of the ground motions from both sources was in agreement and that the peak displacements for the elastic case were two to three times those for the nonlinear case.

The response spectra is compared in Figures 11a through 11e. Their shapes are quite similar at the three farthest ranges and at long periods for the short ranges. The short period response at ranges 5.63 and 16.1 km are very different. One expects that the differences between the linear and nonlinear soil responses to be greatest at high frequencies. Due to the anelastic absorption operator  $e^{-\gamma r}$ , the higher frequency energy is attenuated more with range which therefore suppresses the high frequency differences.

The peak amplitudes and corresponding periods in the response spectra are tabulated in Table 2 and plotted in Figures 12a through 12c. Generally, the peaks for the two source models occur at the same periods. The amplitudes are generally one and one-half to two times greater for the airblast/elastic case than for the full simulation. Thus the nonlinear absorption at the soils beneath the explosion cause the coupling into seismic energy to be reduced by about a factor of two without shifting the periods at which peak motions occur, except at the closest distance.

#### 4.2 THE MIXED PROPAGATION PATH

Recall that in Section II we introduced the mixed propagation path to obtain a transition from the source region to the remainder of the propagation path. The mix of source and receiver path was chosen arbitrarily. We can check the effects of our choice by comparing the motions from

TABLE 2

PERIODS AND AMPLITUDES AT PEAKS IN VERTICAL RESPONSE  
 SPECTRUM FOR THE FULL SIMULATION AND THE  
 AIRBLAST/ELASTIC CASE FOR THE W53 EARTH MODEL

## FULL SIMULATION

## AIRBLAST/ELASTIC

PRD

Range	$T_{max}$	$A_{max}$ (cm)	$T_{max}$	$A_{max}$ (cm)
5.63	2.5	6.0	2.2	11.2
16.1	2.8	1.86	2.8	2.7
56.3	4.0	$1.4 \times 10^{-1}$	4.0	$1.6 \times 10^{-1}$
161.0	5.0	$1.6 \times 10^{-2}$	5.0	$2.2 \times 10^{-2}$
563.0	5.6	$1.3 \times 10^{-3}$	6.3	$2.5 \times 10^{-3}$

PSRV

Range	$T_{max}$	$A_{max}$ (cm/sec)	$T_{max}$	$A_{max}$ (cm/sec)
5.63	2.0	18.0	2.0	34.3
16.1	2.8	4.1	2.2	6.8
56.3	4.0	$2.2 \times 10^{-1}$	4.0	$2.5 \times 10^{-1}$
161.0	5.0	$2.0 \times 10^{-2}$	5.0	$2.8 \times 10^{-2}$
563.0	5.6	$1.5 \times 10^{-3}$	5.6	$2.8 \times 10^{-3}$

PSAA

Range	$T_{max}$	$A_{max}$ (g)	$T_{max}$	$A_{max}$ (g)
5.63	2.0	$5.8 \times 10^{-2}$	1.3	$4.9 \times 10^{-2}$
16.1	2.2	$1.1 \times 10^{-2}$	2.0	$1.9 \times 10^{-2}$
56.3	4.0	$3.5 \times 10^{-4}$	4.0	$4.1 \times 10^{-4}$
161.0	5.0	$2.6 \times 10^{-5}$	5.0	$3.6 \times 10^{-5}$
563.0	5.6	$1.7 \times 10^{-6}$	5.6	$3.2 \times 10^{-6}$

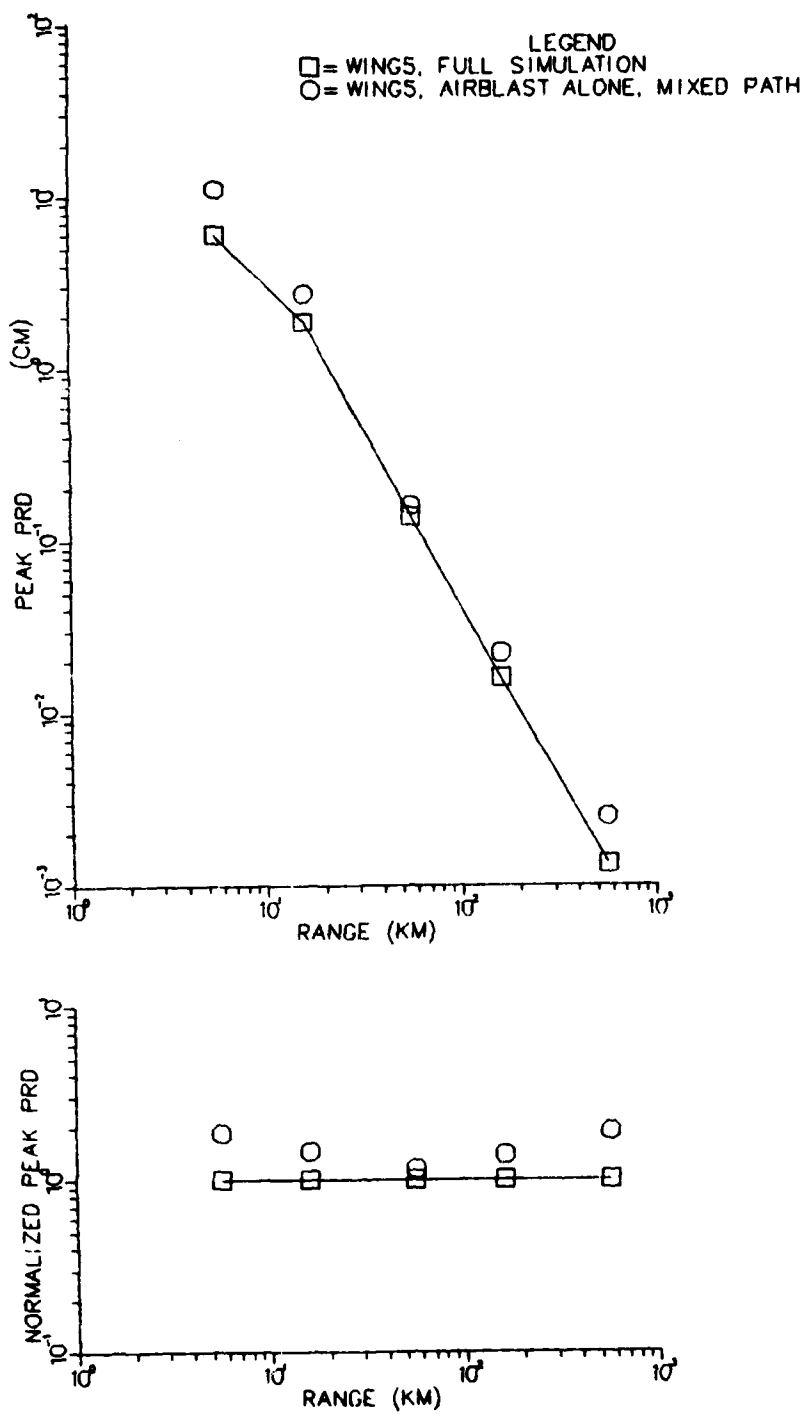


Figure 12a. Peak values in PRD are plotted versus range for the full simulation and the airblast/elastic case. In the lower plot, the values are normalized to those of the full simulation.

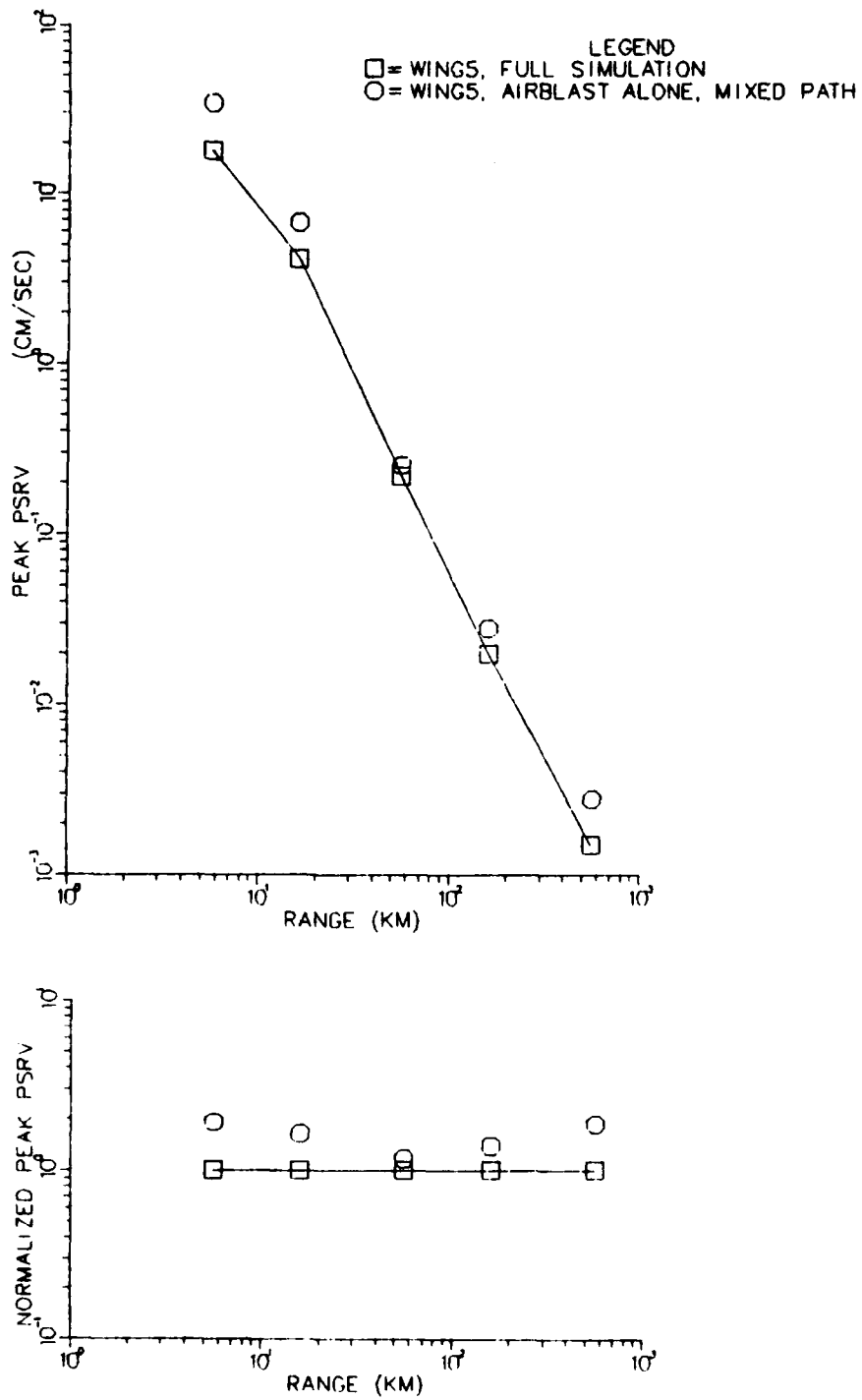


Figure 12b. Peak values of PSRV are plotted versus range for the full simulation and the airblast/elastic case. In the lower plot, the values are normalized to those of the full simulation.

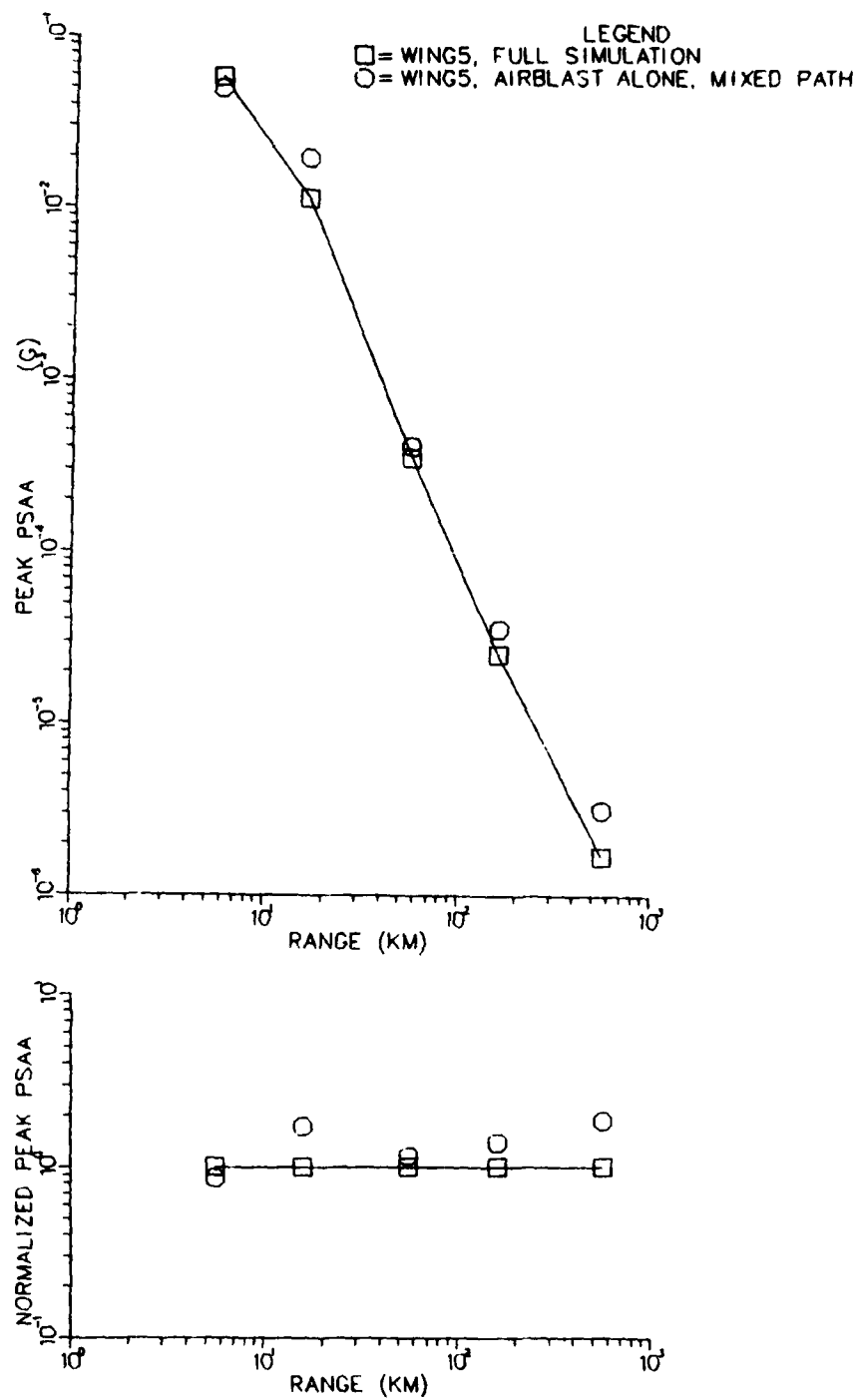


Figure 12c. Peak values of PSAA are plotted versus range for the full simulation and the airblast/elastic case. In the lower plot, the values are normalized to those of the full simulation.

the airblast/elastic source with and without the mixed path. That is, we compare the above results discussed with those for which the source region radius  $R_s$  goes to zero. The medium is then a simple layered halfspace and no transition is needed.

We again use the W5S3 structure. Figure 13 shows the synthetic seismograms for the single path. These should be compared with the seismograms in Figure 10. The response spectra are compared in Figures 14a through 14e and peaks are plotted versus range in Figures 15a through 15c. The seismogram shapes are similar and, except at the smallest distance, the peak displacements are close to those obtained from the seismograms in Figure 10. The peak response spectra agree well except for the PSAA at 5.63 km. This peak occurs below the one second cutoff and is not reliable. If, instead, we use the value at 1.2 seconds where the mixed path spectrum peaked, the ratio of the single path to mixed path peaks is about three. Since the path is mixed only in the top 600 m, we expect its effects to be seen only at high frequencies and small ranges which is the case. So except for the accelerations at  $r = 5.63$ , our choice of source region dimension is not important and for the purpose of computing ground motions for the airblast/elastic case we can use the simpler single path model.

#### 4.3 COMPARISON OF GROUND MOTIONS FOR THREE EARTH STRUCTURES

In this section we explore the differences in response of the three crustal structures discussed in Section II (Figures 3 and 4). For these calculations we have used the airblast/elastic source and the single propagation path.

Note that the structures are very close to being the same below about 10 km (Figure 3) so that differences in response must be due largely to differences above that depth.

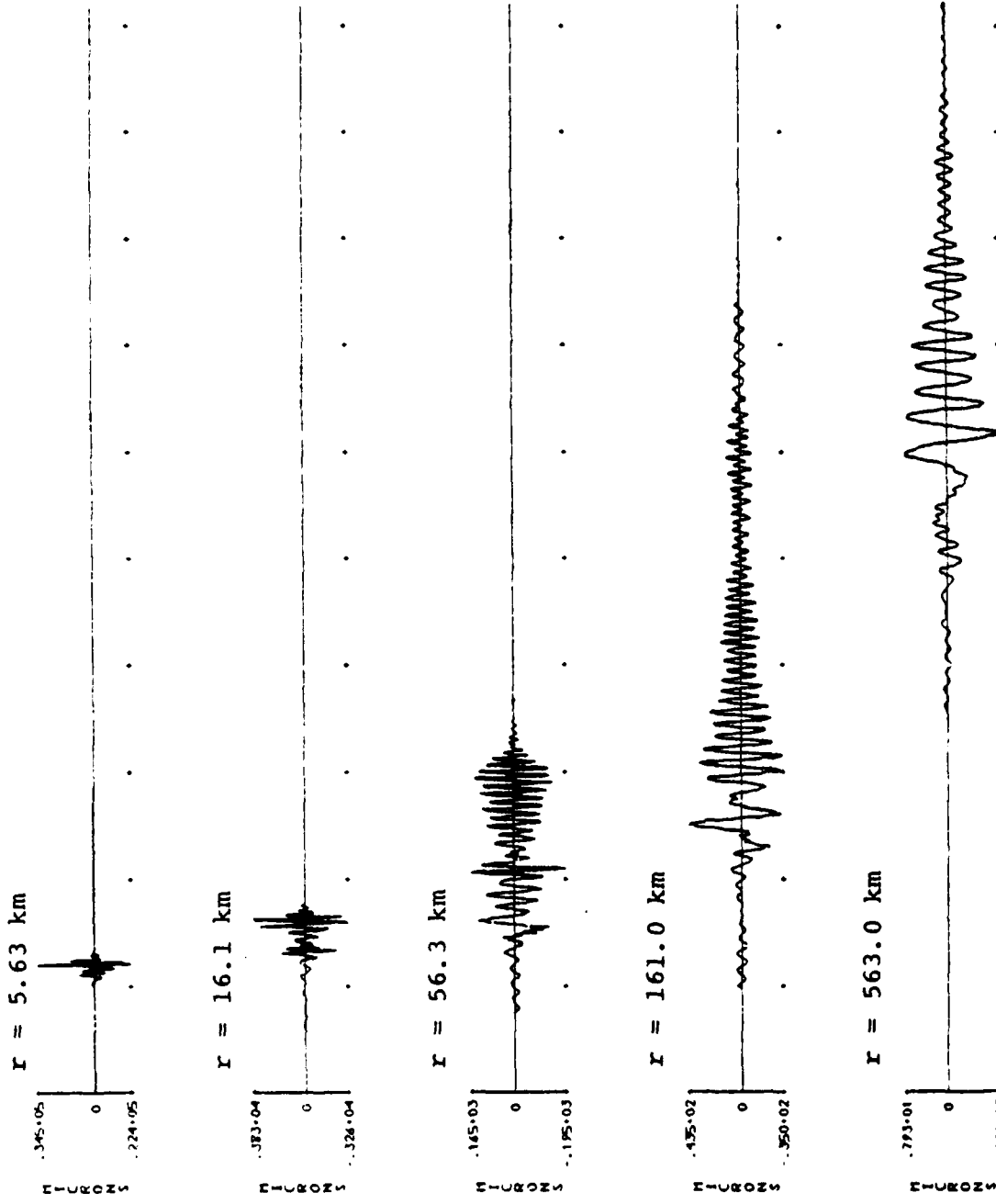


**Figure 13.** Synthetic displacement seismograms for the airblast/elastic case with a single propagation path are shown. Tick marks are at 40 second intervals, beginning at -40 seconds.

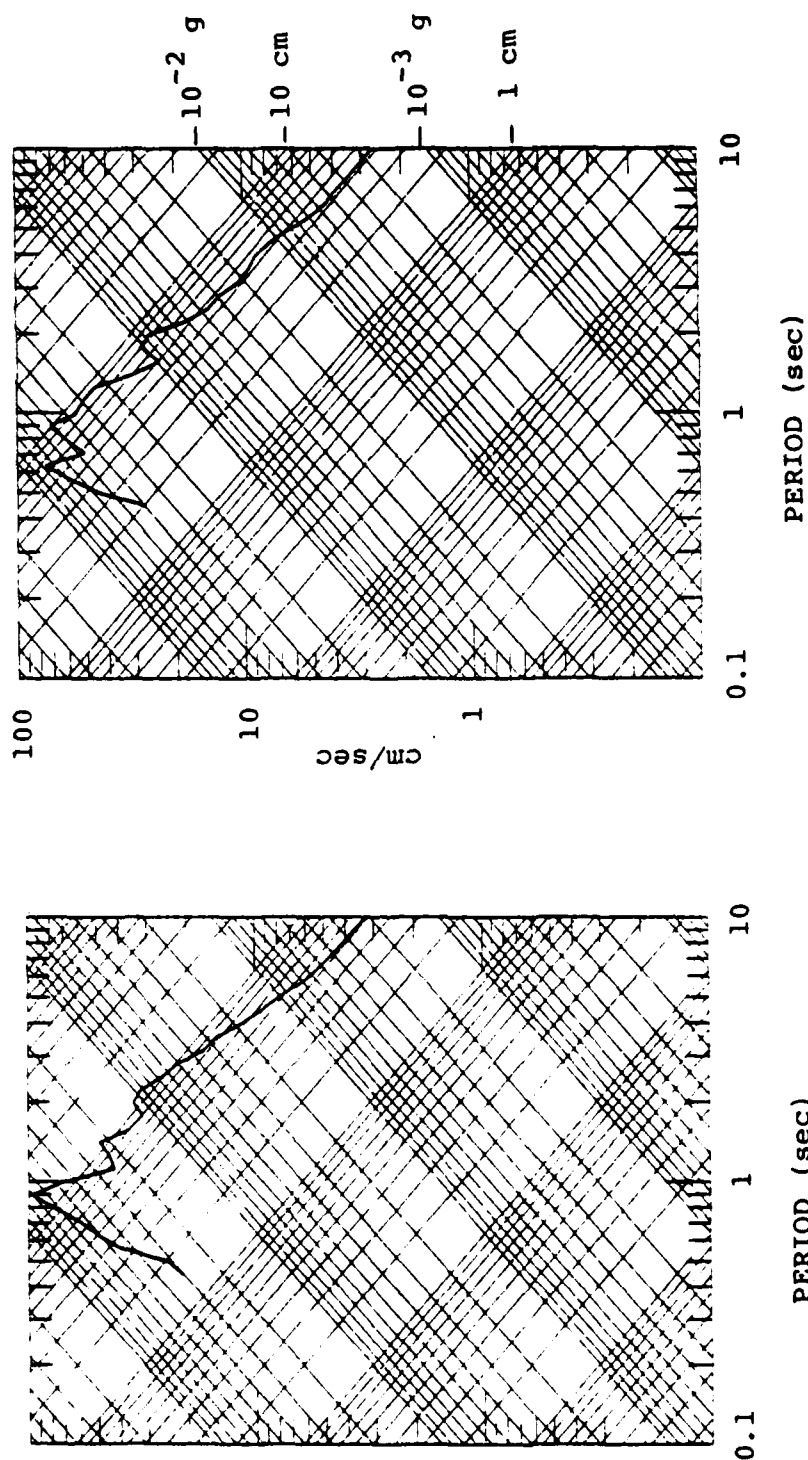


Figure 14a. Response spectra for the airblast on an elastic medium for the mixed path (left) and for the single path are shown;  $r = 5.63$  km.

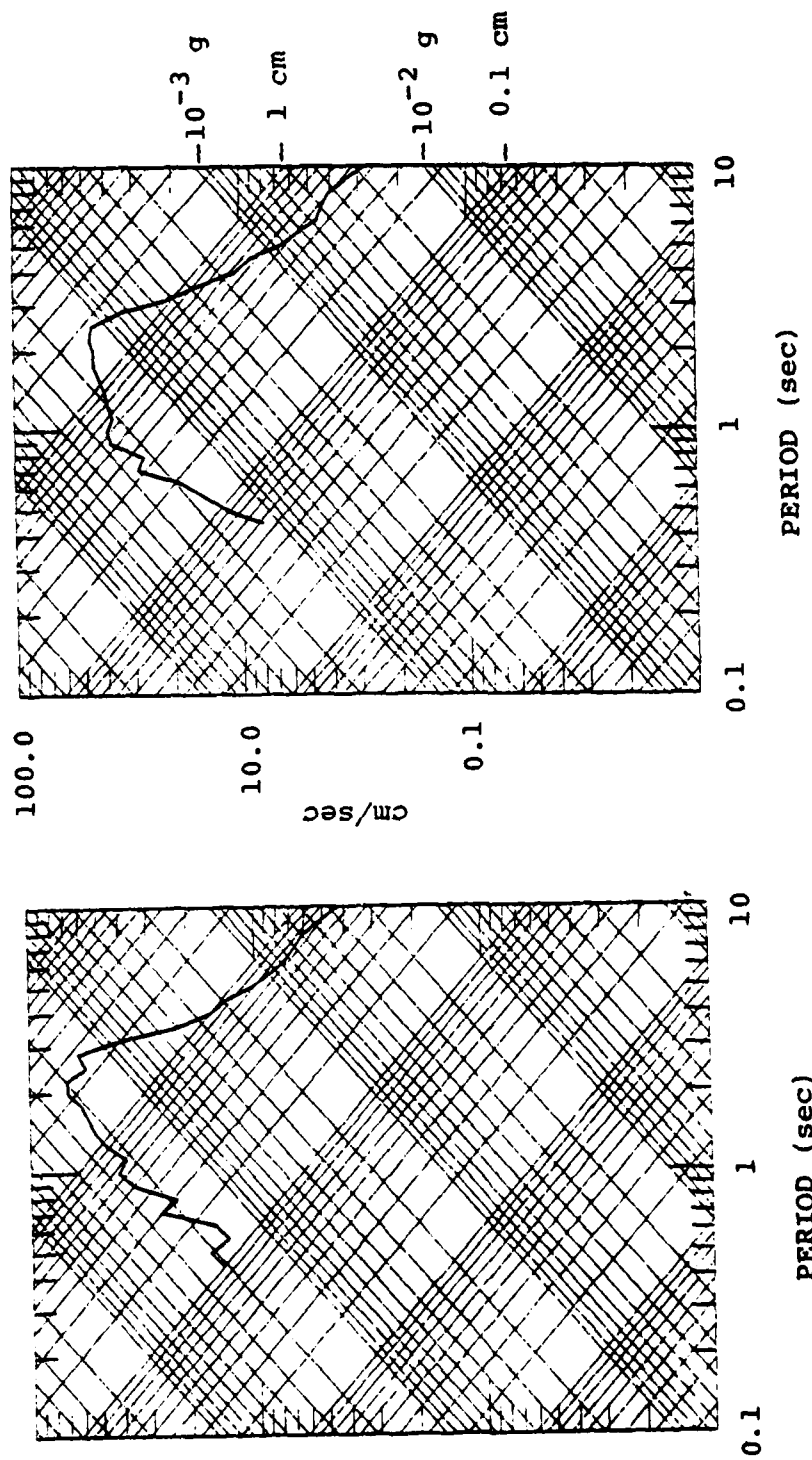


Figure 14b. Response spectra for the airblast on an elastic medium for the mixed path (left) and for the single path are shown;  
 $r = 16.1$  km.

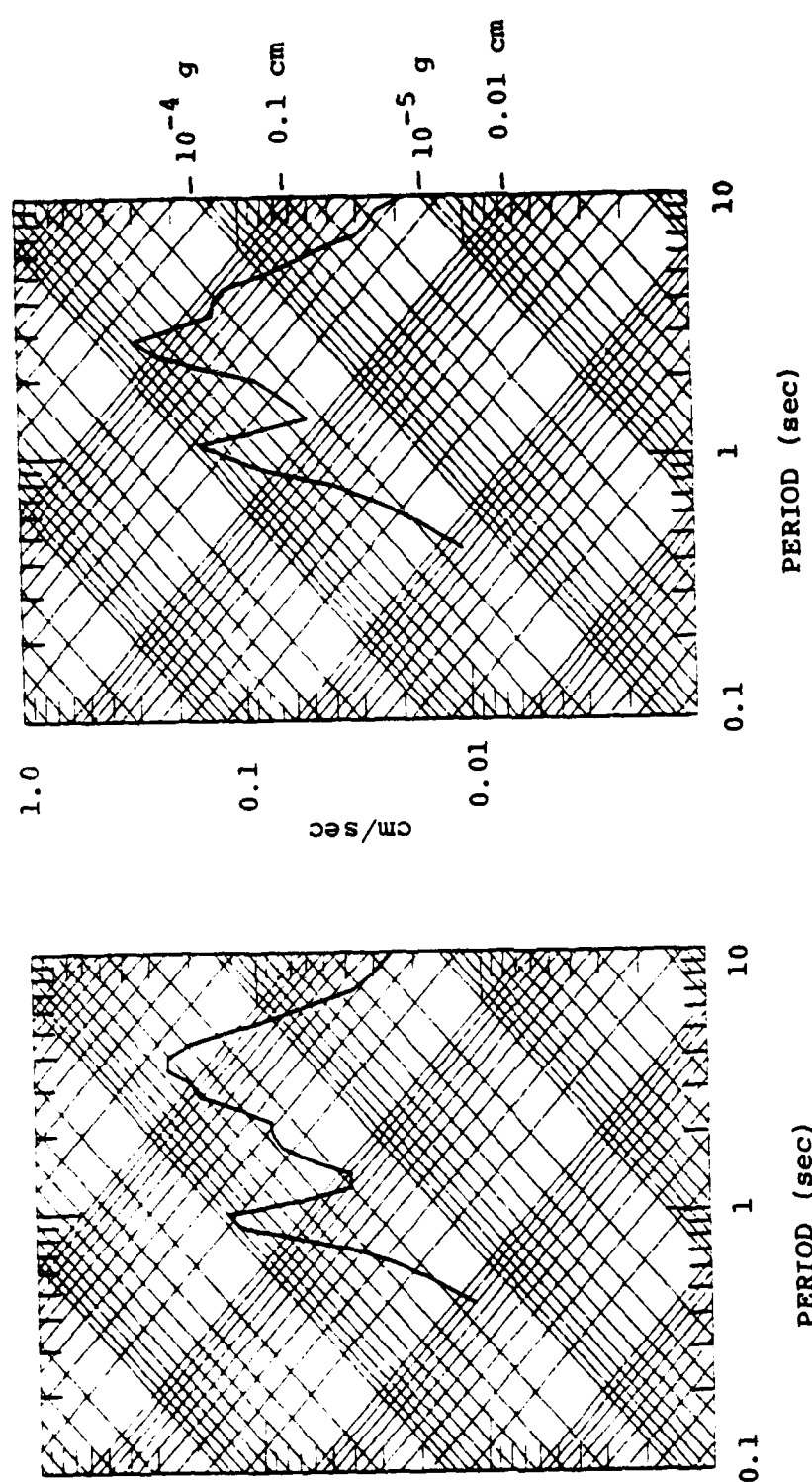


Figure 14c. Response spectra for the airblast on an elastic medium for the mixed path (left) and for the single path are shown;  
 $r = 56.3$  km.

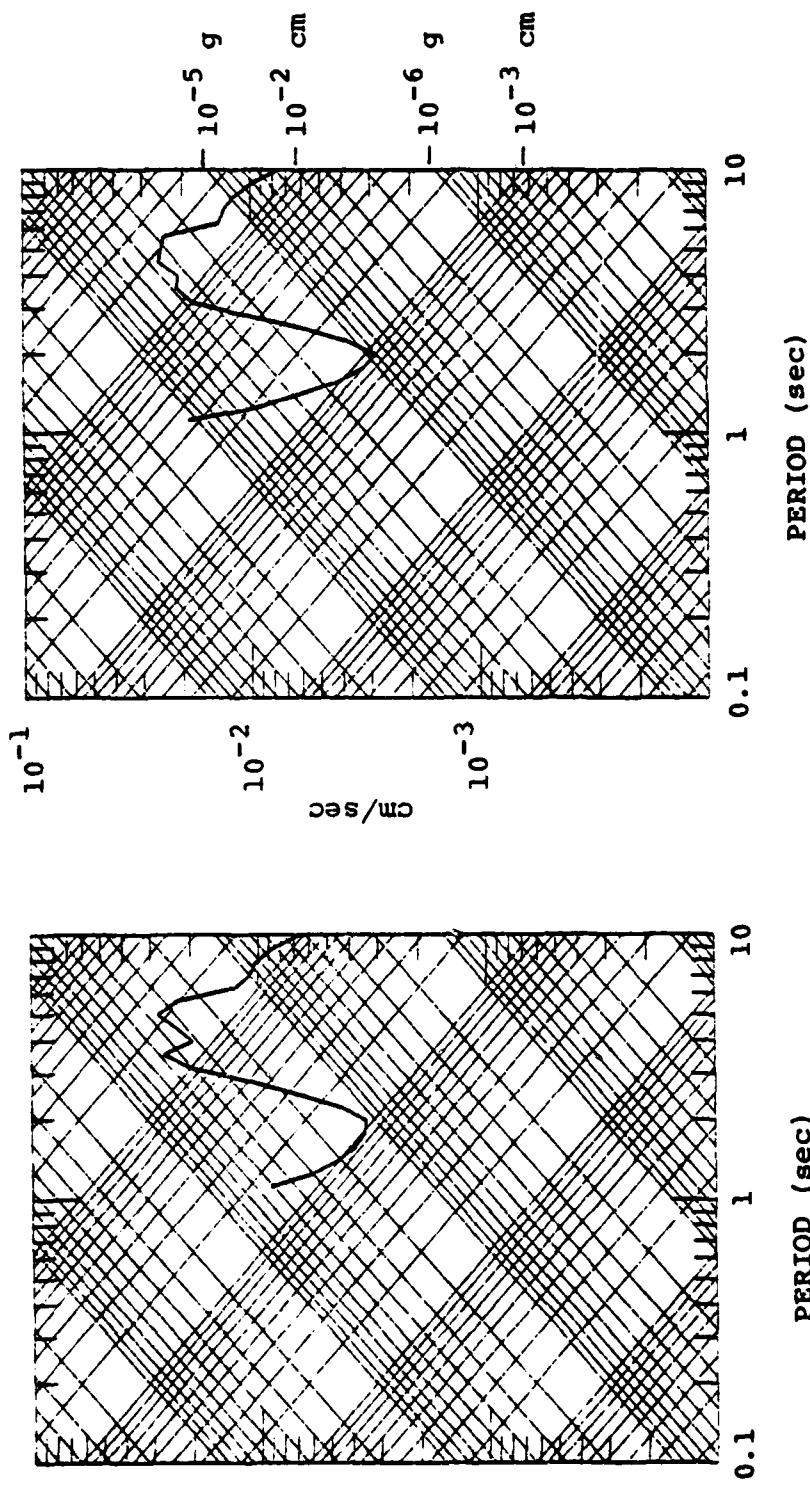


Figure 14d. Response spectra for the airblast on an elastic medium for the mixed path (left) and for the single path are shown;  
 $r = 161.0$  km.

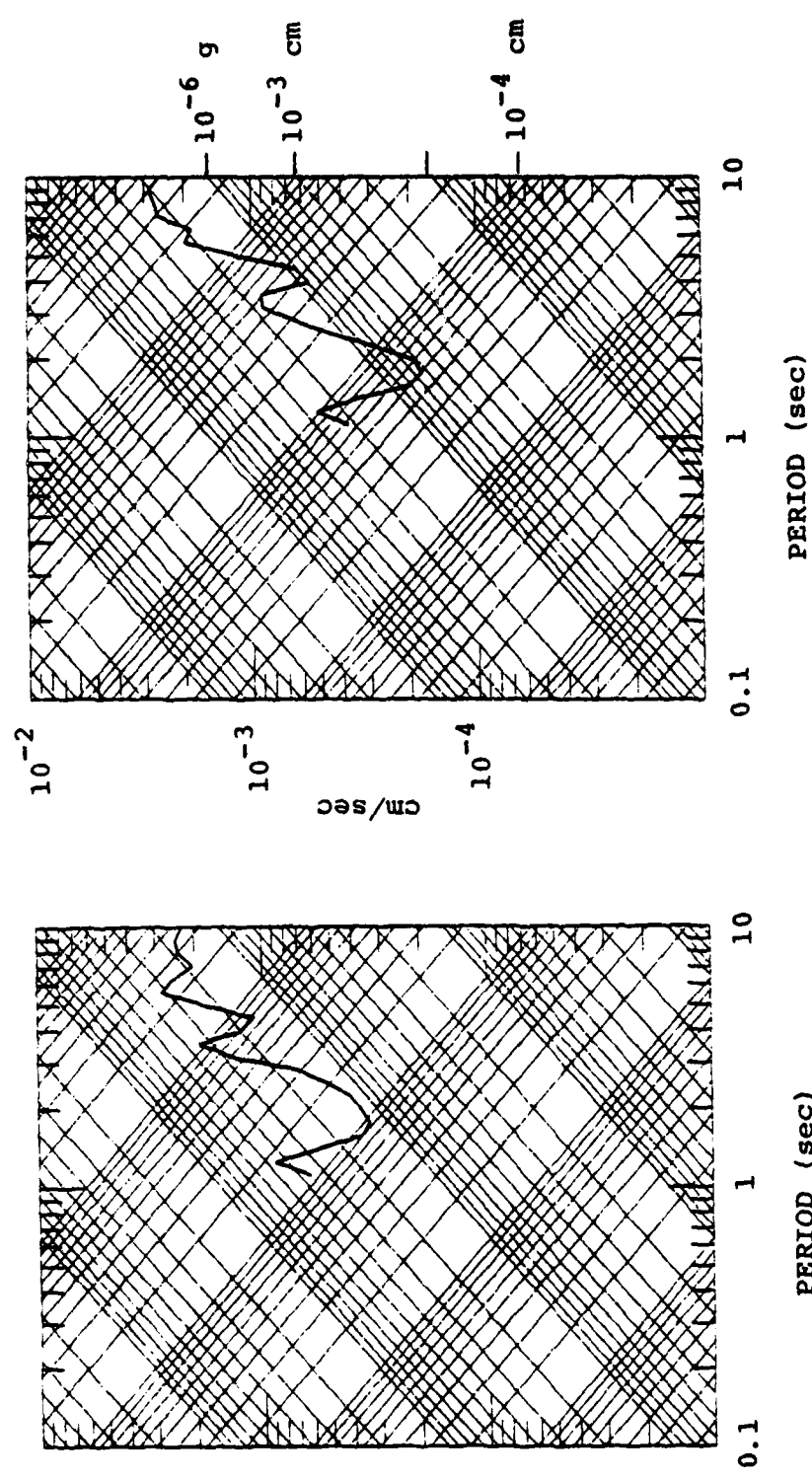


Figure 14e. Response spectra for the airblast on an elastic medium for the mixed path (left) and for the single path are shown;  
 $r = 563.0$  km.

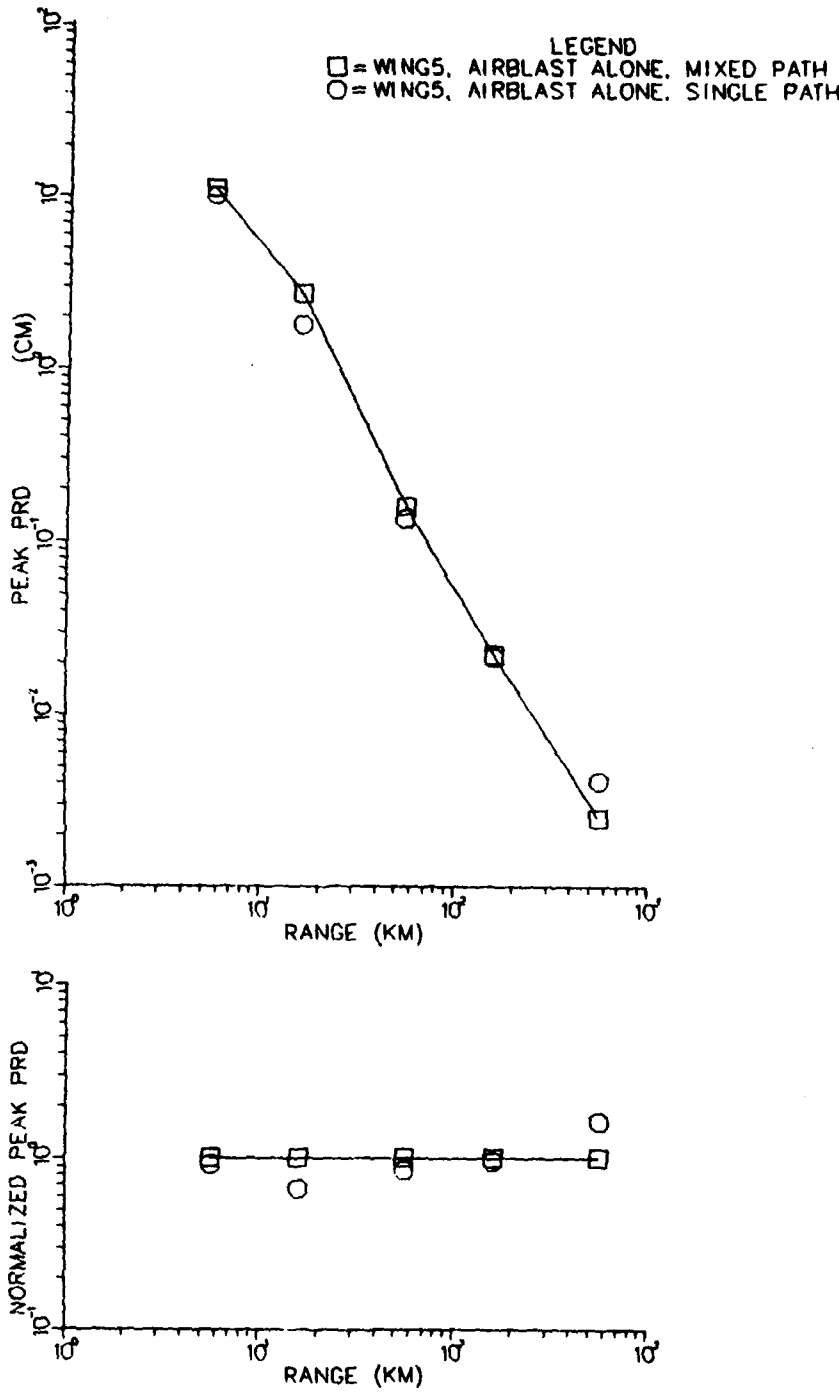
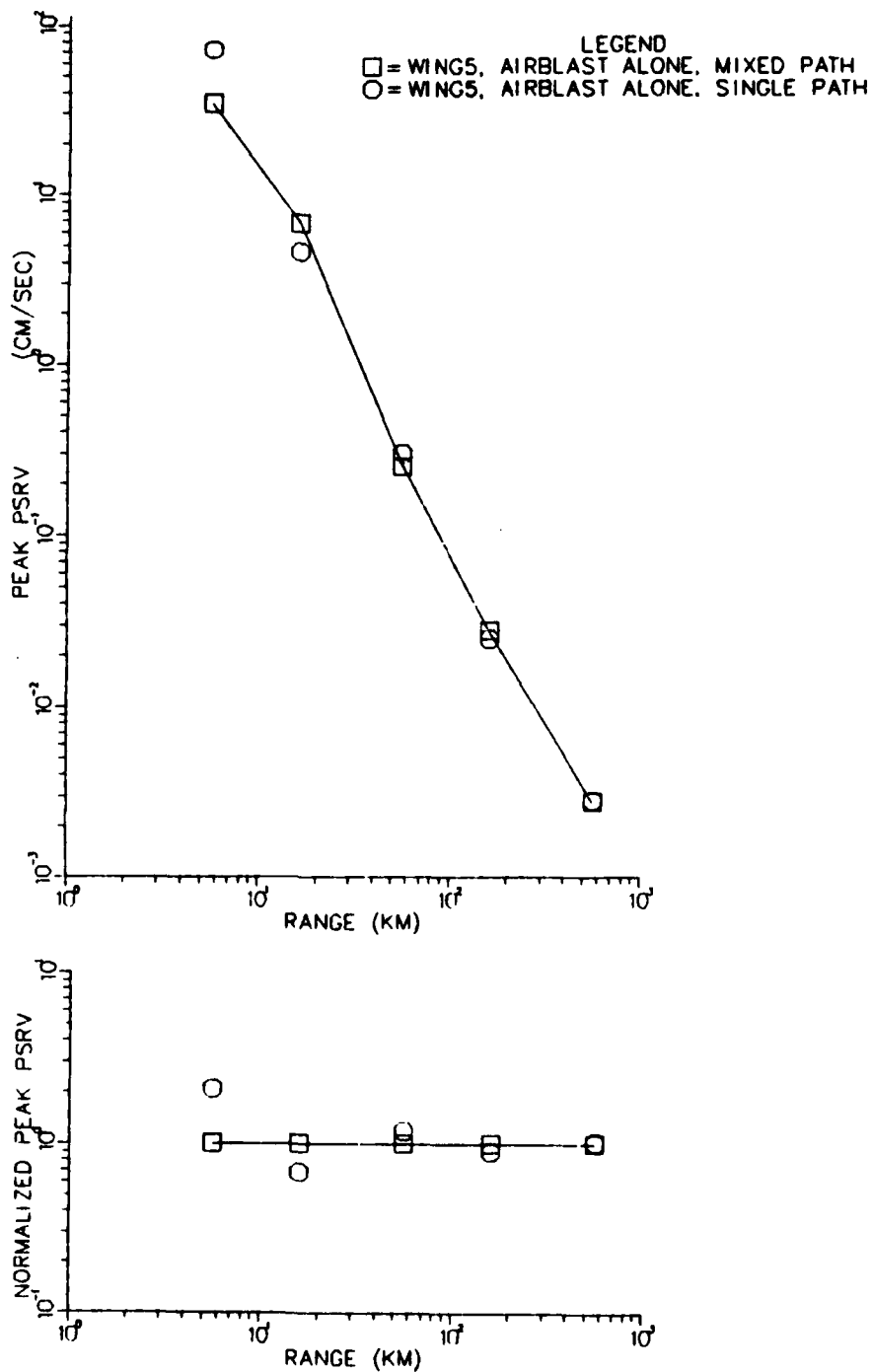


Figure 15a. Peak values of PRD are plotted versus range for the airblast/elastic source with a single and a mixed propagation path. Values in bottom plot are normalized to the mixed path values.



**Figure 15b.** Peak values of PSRV are plotted versus range for the airblast/elastic source with a single and a mixed propagation path. Values in bottom plot are normalized to the mixed path values.

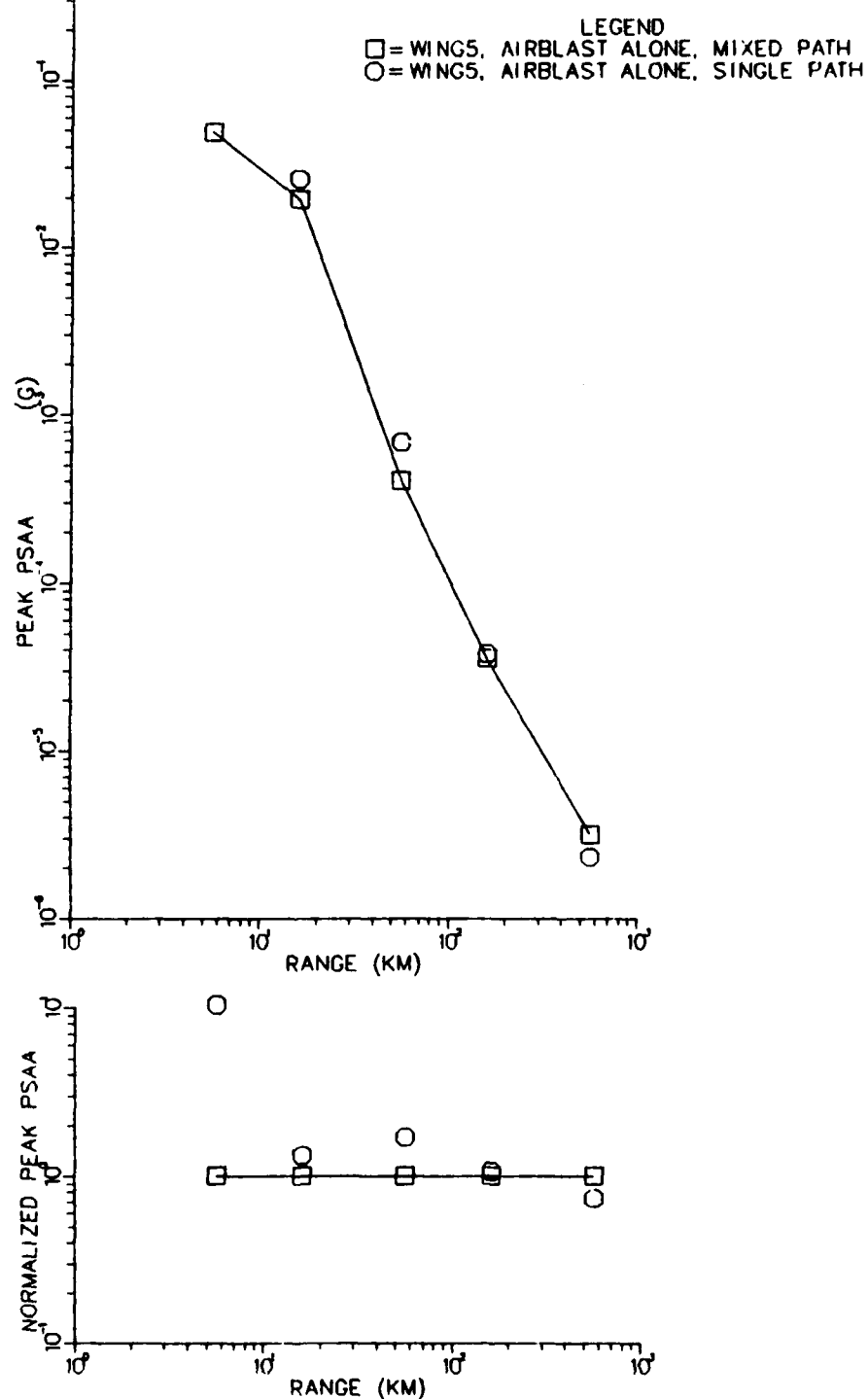


Figure 15c. Peak values of PSAA are plotted versus range for the airblast/elastic source with a single and a mixed propagation path. Values in bottom plot are normalized to the mixed path values.

At W5S3 and W6S1, the shear wave speeds ( $\beta$ ) are very low at the surface (0.6 to 0.7 km/sec). W5S3 has a relatively gradual increase in  $\beta$  compared to W6S1 which quadruples its value within 1 km of the surface. At W4S8, the surface value of  $\beta$  is 1.8 km/sec, increases to 3.2 km/sec in the upper 1 km and gradually increases below that.

The most obvious differences in the synthetic seismograms (Figures 16 through 18) is the signal duration at W4S8 compared to W6S1 and W5S3. At all ranges, the signal at W4S8 is rather pulse like without the later time ringing evident at the other sites. The ringing is due to waves traveling in the slow upper 1 km of crust at W5S3 and W6S1.

Differences in excitation of the crustal structure are very apparent in the response spectra compared in Figures 19a through 19e. Amplitudes and periods of spectral peaks are given in Table 3 and amplitudes are plotted in Figures 20a through 20c. For the most part, the response spectra peak in the period range of interest (one to ten seconds). Peaks in the response spectra at W5S3 occur at longer periods than at the other wings, while the peaks at W6S1 and W4S8 occur at roughly the same period (except at the closest receiver). The dominance of energy at longer periods at W5S3 is due to the gradual increase in  $\beta$  in the upper 6 km of the crust relative to the other sites.

From Figures 20a through 20c, we see a tendency for peak spectral amplitudes at W4S8 and W6S1 to increase relative to W5S3 as a function of range. The values of peak PSRV at W4S8 and W6S1 are within a factor of two of those at W5S3. The PRD and PSAA peaks differ by as much as a factor of four, with the greatest difference in close for the PRD peaks and at the greater ranges for the PSAA.

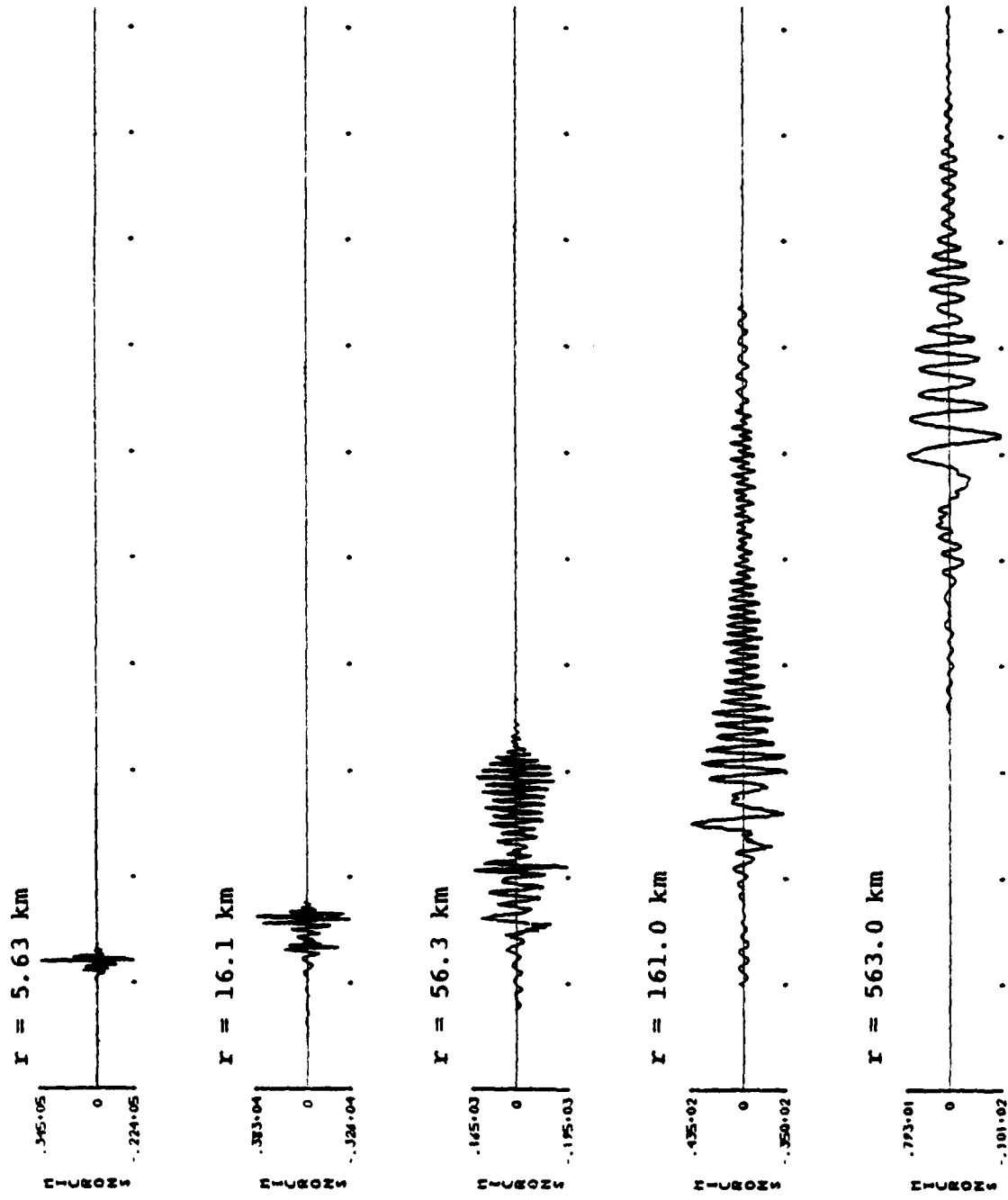


Figure 16. Synthetic displacement seismograms at W5S3 for the airblast/elastic case with a single propagation path are shown. Tick marks are at 40 second intervals, beginning at -40 seconds.

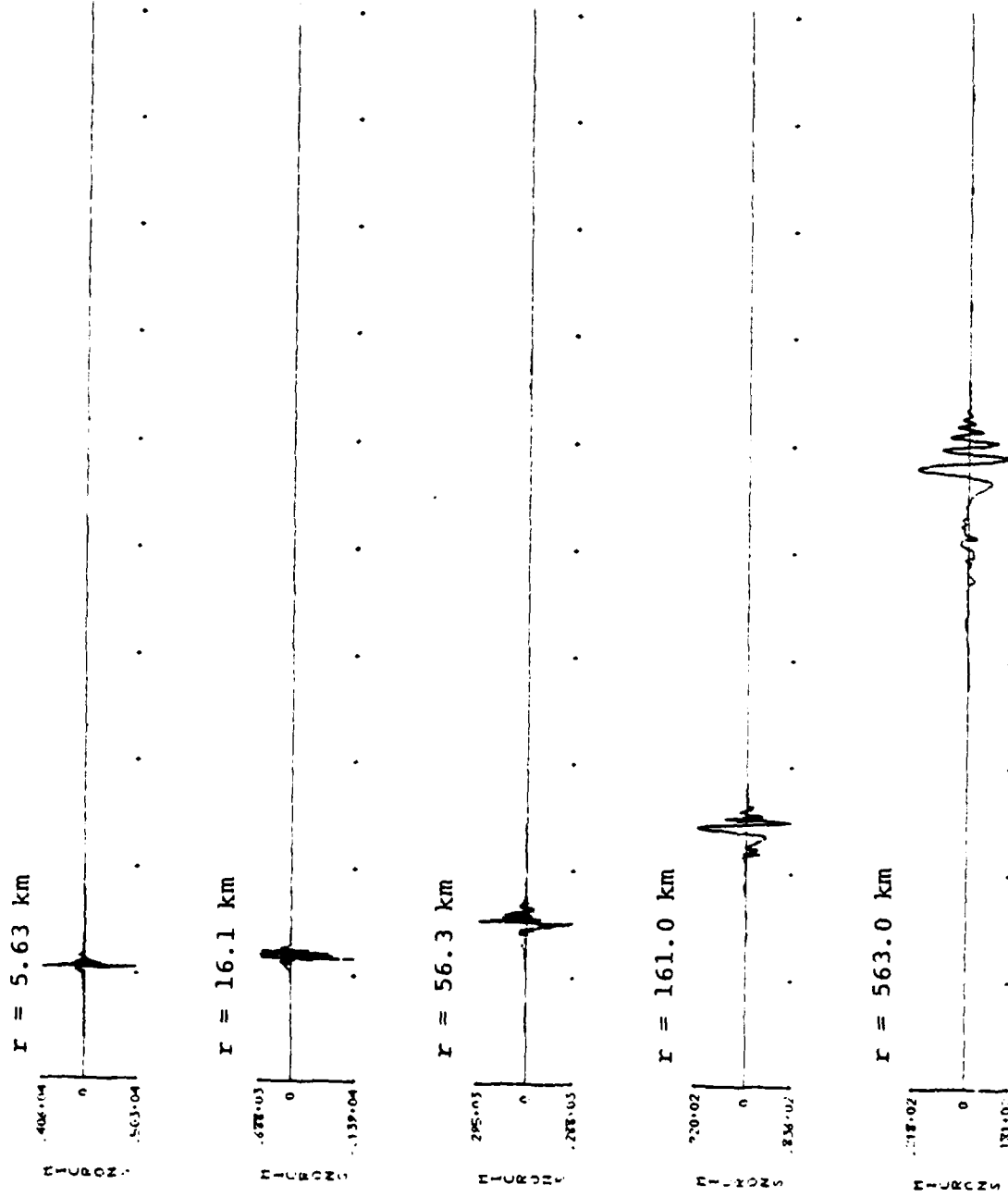


Figure 17. Synthetic displacement seismograms at W4S8 for the airblast/elastic case with a single propagation path are shown. Tick marks are at 40 second intervals, beginning at -40 seconds.

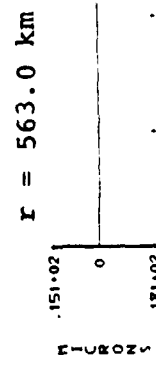
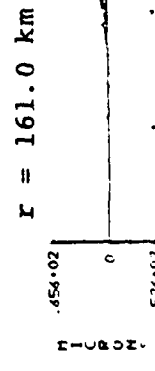
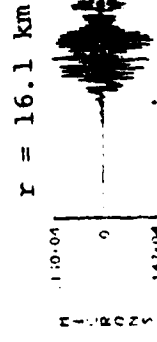
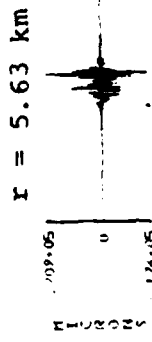


Figure 18. Synthetic displacement seismograms at W6S1 for the airblast/elastic case with a single propagation path are shown. Tick marks are at 40 second intervals, beginning at -40 seconds.

TABLE 3

PERIODS AND AMPLITUDES AT PEAKS IN VERTICAL RESPONSE  
SPECTRA FOR THE AIRBLAST-ALONE SOURCE AT THE  
THREE WINGS USING SINGLE PATH PROPAGATION

Range	<u>PRD</u>				<u>PSRV</u>				<u>PSAA</u>			
	W5S3		W4S8		W6S1		W5S3		W4S8		W6S1	
	T <sub>max</sub>	A <sub>max</sub>	T <sub>max</sub>	A <sub>max</sub>	T <sub>max</sub>	A <sub>max</sub>		T <sub>max</sub>	A <sub>max</sub>	T <sub>max</sub>	A <sub>max</sub>	
5.63	0.9	$1.0 \times 10^5$	0.5	$2.6 \times 10^4$	1.0	$8.3 \times 10^4$						
16.1	2.5	$1.8 \times 10^4$	0.7	$5.2 \times 10^3$	1.3	$1.1 \times 10^4$						
56.3	2.8	$1.4 \times 10^3$	2.0	$7.7 \times 10^2$	1.7	$7.8 \times 10^2$						
161.0	5.6	$2.1 \times 10^2$	3.6	$2.2 \times 10^2$	5.6	$2.0 \times 10^2$						
563.0	10.0	$4.1 \times 10^1$	7.1	$7.3 \times 10^1$	6.3	$7.6 \times 10^1$						
5.63	0.9	$7.2 \times 10^5$	0.5	$3.7 \times 10^5$	1.0	$5.2 \times 10^5$						
16.1	2.2	$4.6 \times 10^4$	0.7	$4.6 \times 10^4$	1.3	$5.4 \times 10^4$						
56.3	2.8	$3.0 \times 10^3$	1.1	$3.3 \times 10^3$	1.6	$3.1 \times 10^3$						
161.0	4.5	$2.5 \times 10^2$	2.5	$4.8 \times 10^2$	3.2	$2.7 \times 10^2$						
563.0	8.9	$2.8 \times 10^1$	5.62	$7.0 \times 10^1$	5.6	$8.0 \times 10^1$						
5.63	0.7	$5.1 \times 10^6$	0.5	$3.7 \times 10^5$	0.7	$4.3 \times 10^6$						
16.1	0.7	$2.5 \times 10^5$	0.5	$4.8 \times 10^5$	1.3	$2.7 \times 10^5$						
56.3	2.8	$6.7 \times 10^3$	1.0	$1.9 \times 10^4$	1.6	$1.2 \times 10^4$						
161.0	3.6	$3.7 \times 10^2$	1.8	$1.5 \times 10^3$	3.2	$5.3 \times 10^2$						
563.0	7.1	$2.3 \times 10^1$	4.5	$8.5 \times 10^1$	4.5	$9.7 \times 10^1$						

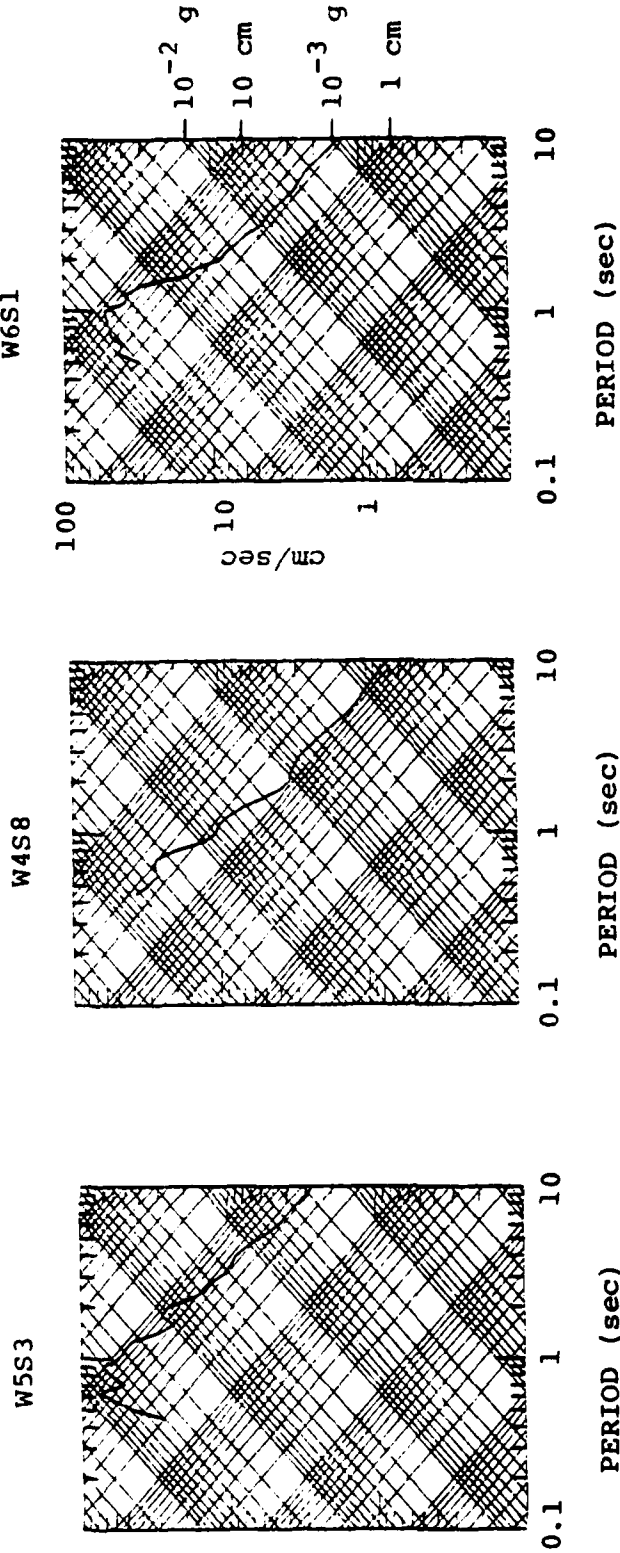


Figure 19a. Response spectra for the airblast/elastic case with a single propagation path are shown for the three sites at  $r = 5.63$  km.

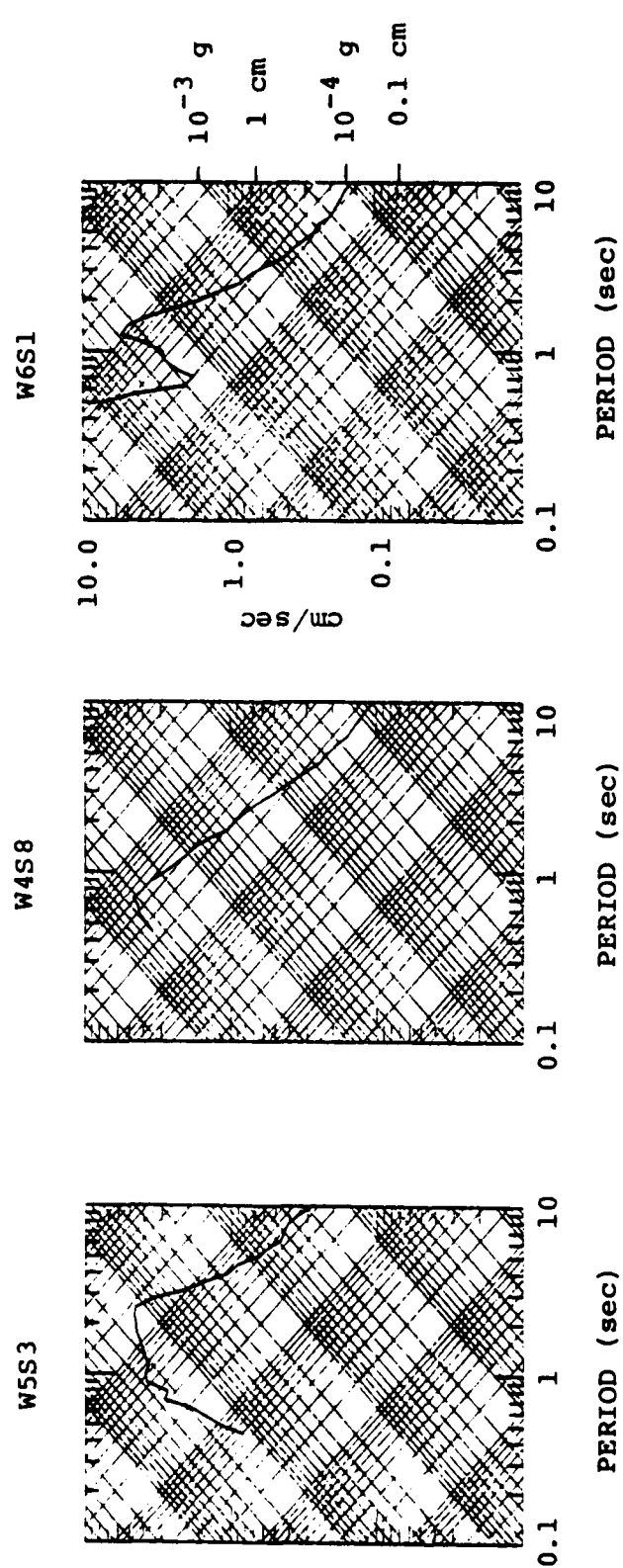


Figure 19b. Response spectra for the airblast/elastic case with a single propagation path are shown for the three sites at  $r = 16.1$  km.

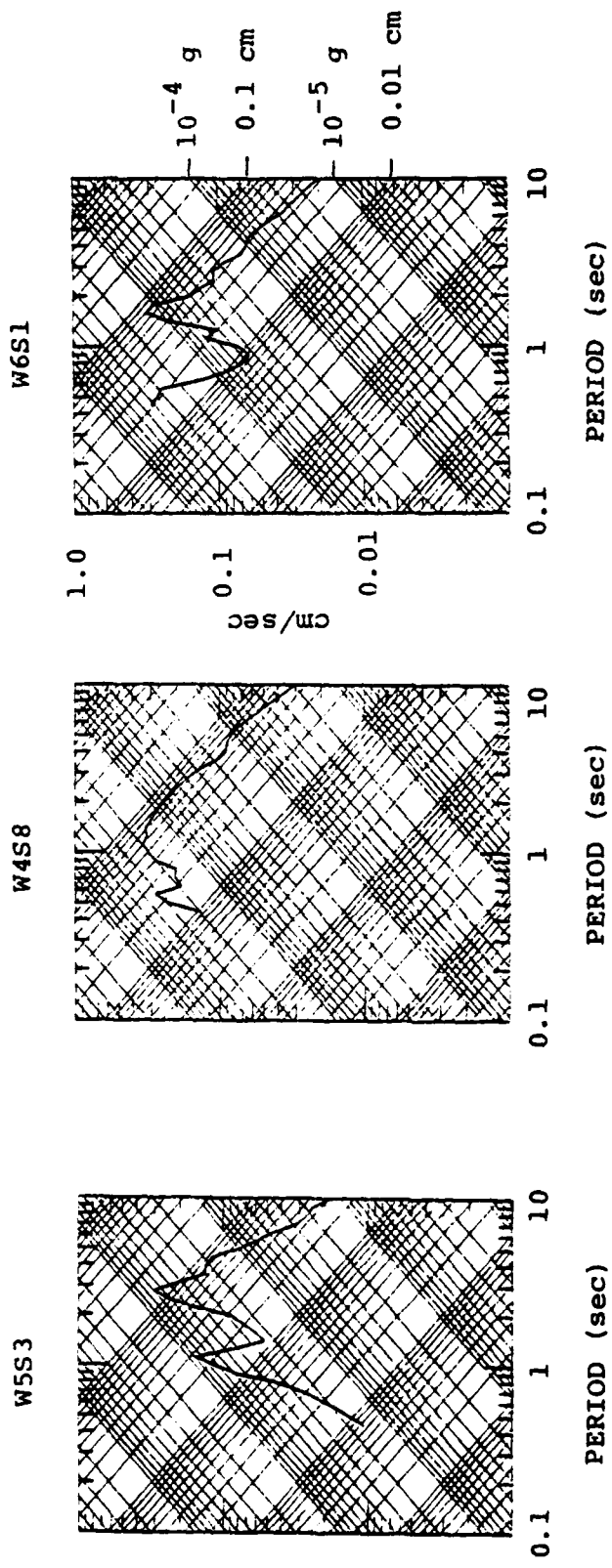


Figure 19c. Response spectra for the airblast/elastic case with a single propagation path are shown for the three sites at  $r = 56.3$  km.

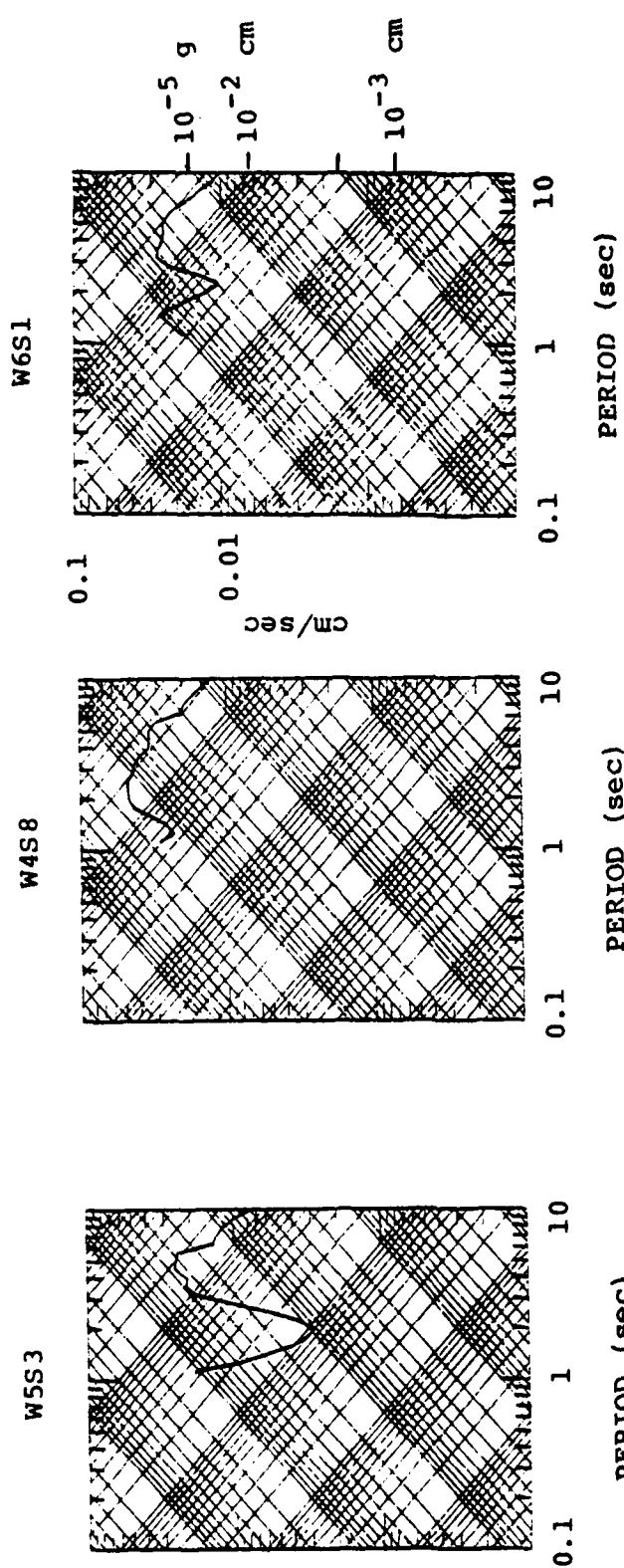


Figure 19d. Response spectra for the airblast/elastic case with a single propagation path are shown for the three sites at  $r = 161.0$  km.

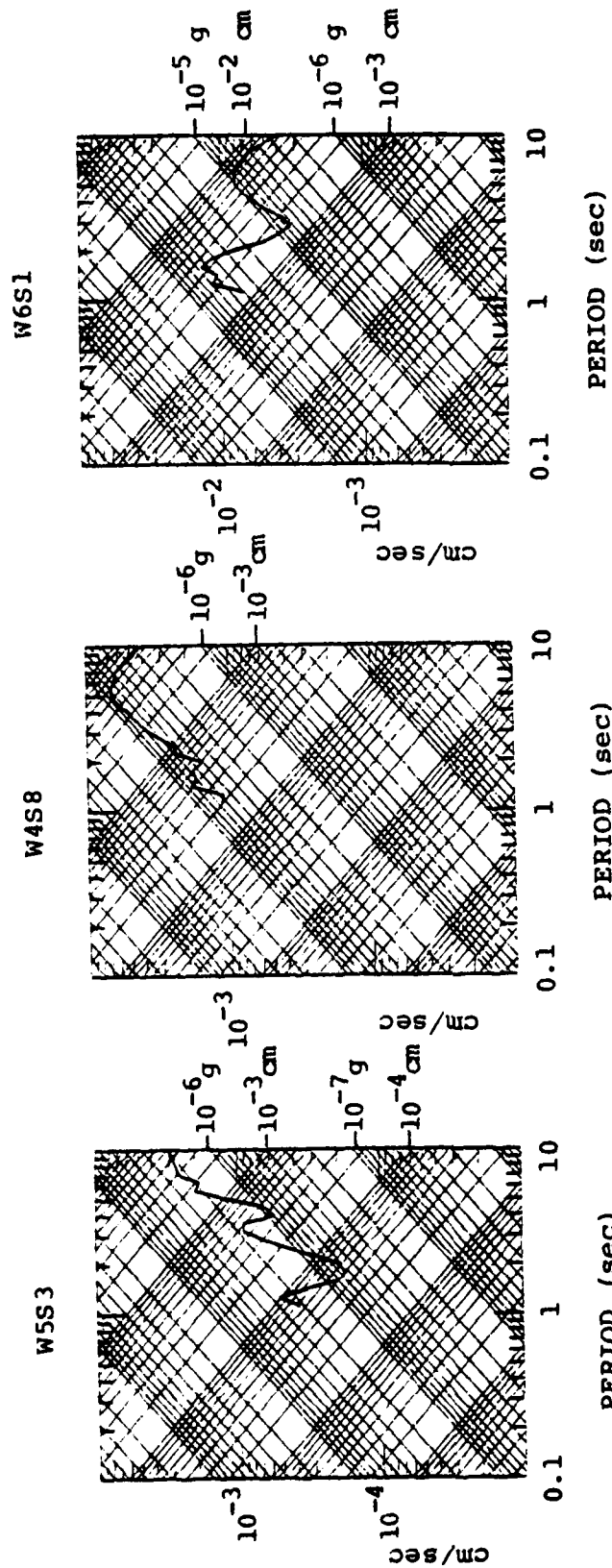


Figure 19e. Response spectra for the airblast/elastic case with a single propagation path are shown for the three sites at  $r = 563.0$  km.

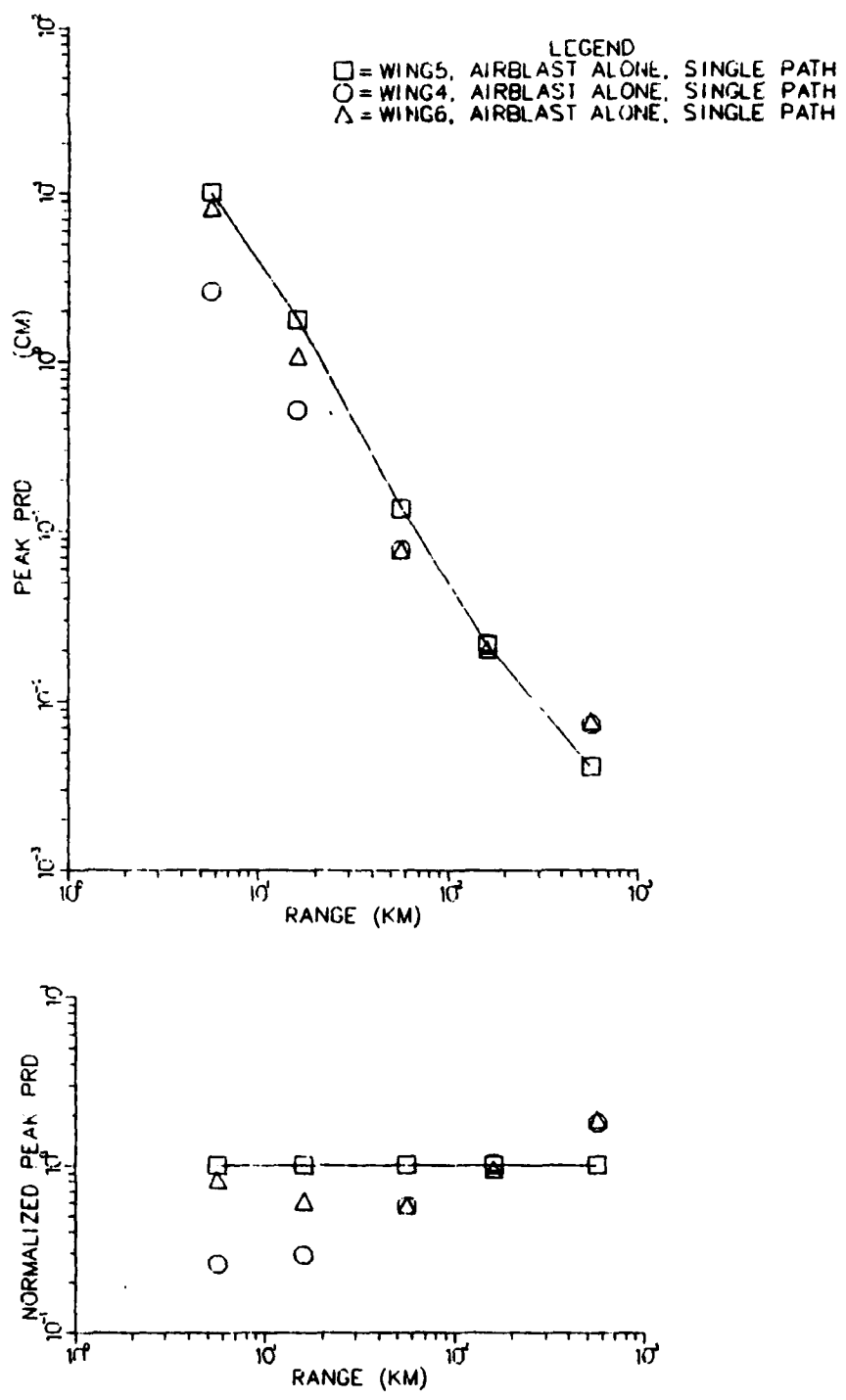


Figure 20a. Peak values of PRD are plotted versus range for W5S3, W4S8 and W6S1. Values are normalized to W5S3 in the bottom plot.

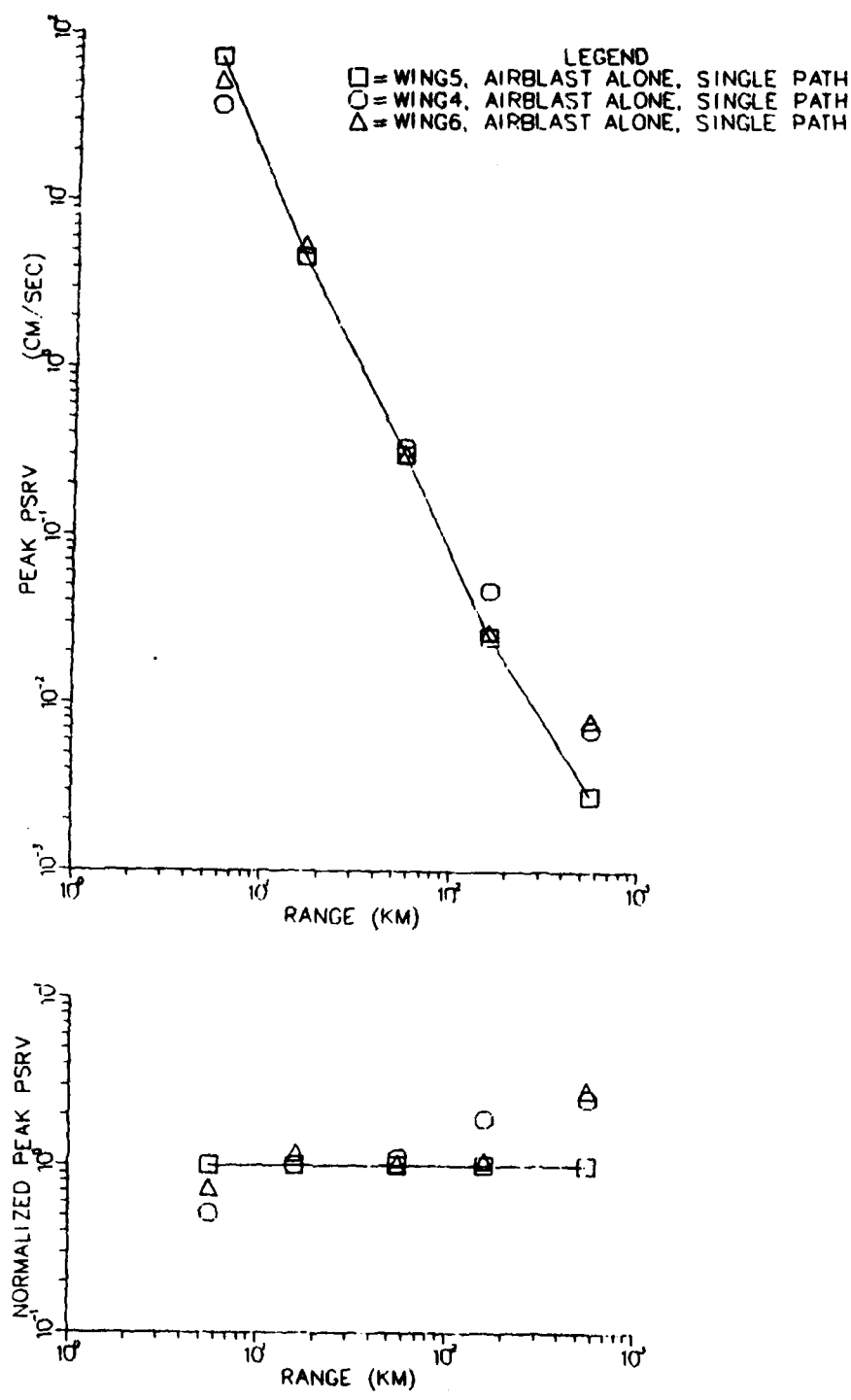


Figure 20b. Peak values of PSRV are plotted versus range for W5S3, W4S8 and W6S1. Values are normalized to W5S3 in the bottom plot.

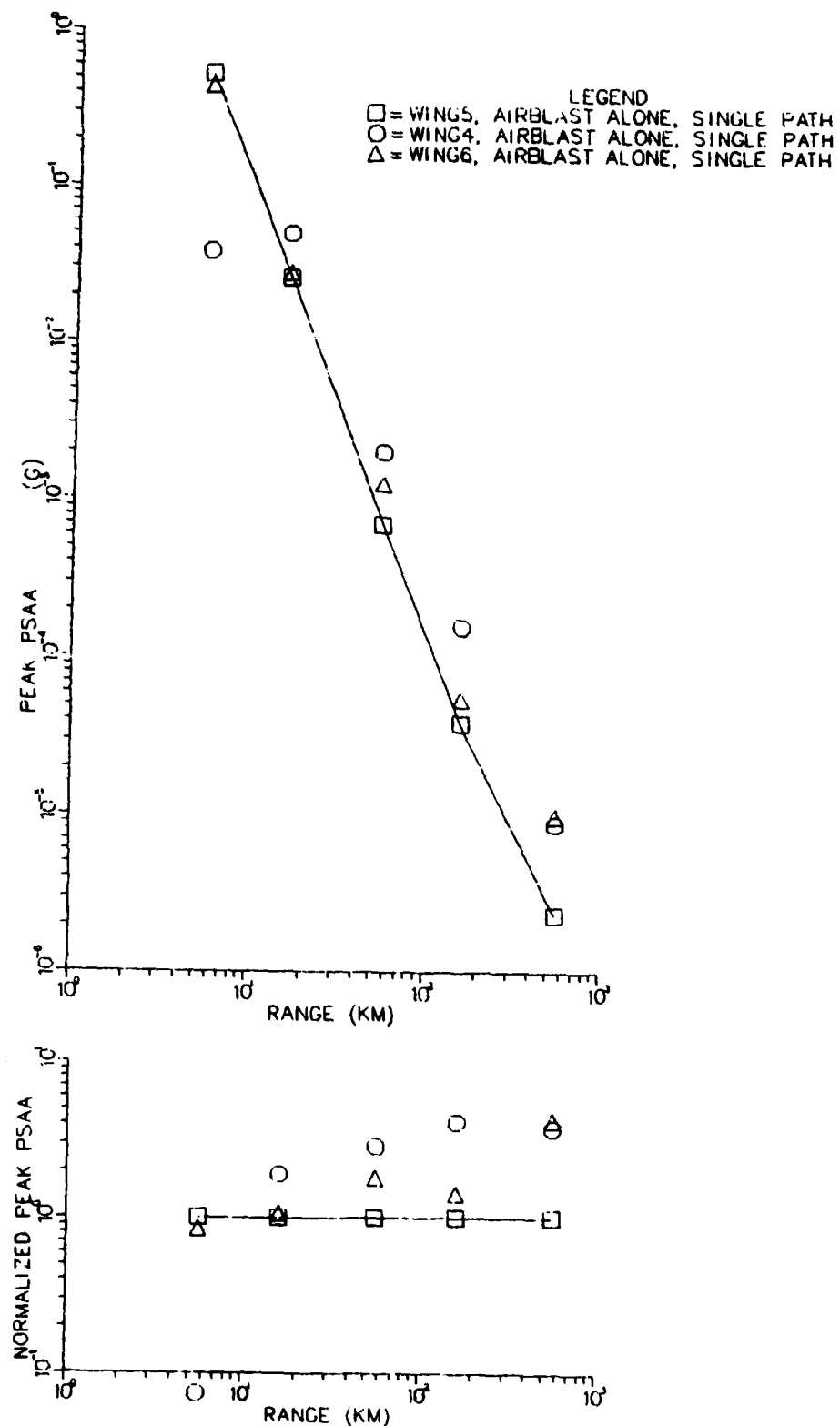


Figure 20c. Peak values of PSAA are plotted versus range for W5S3, W4S8 and W6S1. Values are normalized to W5S3 in the bottom plot.

#### 4.4 DEPENDENCE ON Q

The Q models described in Section III were derived from a body of evidence which constrains the relative values of Q within the stack of layers considerably more than their absolute values. To provide a bound on the greatest likely attenuation we have computed seismograms for the W5S3 crustal structure in which all values of Q have been halved (or equivalently, the values of  $\gamma$  doubled). The airblast/elastic source and the single path propagation model have been used.

A list comparing amplitudes and periods of peaks in the response spectra for the Q model in Table 1 and for the half-Q model is given in Table 4. Peak amplitudes versus range are shown in Figures 2la through 2lc.

The periods  $T_{\max}$  shift very little for the PRD and PSRV for all ranges and for the PSAA at the closer ranges. The peaks are attenuated at the two farthest stations by factors ranging from 1.3 to 2.6, and by factors as large as 5.6 at the three inner stations. The inner ranges are affected more because the parameter  $\gamma$  is a rapidly increasing function of frequency. For example, the value of  $\gamma$  for the fundamental mode at 8.9 seconds is  $5.1 \times 10^{-4}$  km while at 0.9 seconds,  $\gamma$  is  $1.7 \times 10^{-1}$  km. Thus at  $r = 5.63$ , where the response spectra peaks at 0.9 seconds, the attenuation due to doubling  $\gamma$  is about  $e^{-\gamma r}/e^{-\gamma r}$ , or 0.38. At  $r = 5.63$  km on the other hand the peak is at 8.9 seconds and is reduced by 0.75, about half the reduction seen at 5.63 km.

It is well known that the Q model is a critical parameter required for an accurate estimate of seismic ground motion. Recently new techniques have become available for determining Q on a site specific basis. Consideration should be given to their application to those sites where ground motion predictions of the type discussed here are required.

TABLE 4

PERIODS AND AMPLITUDES AT PEAKS IN VERTICAL RESPONSE  
 SPECTRA FOR THE AIRBLAST ALONE SOURCE AT WING 5  
 FOR THE Q MODEL IN FIGURE 5 AND FOR  
 THAT MODEL WITH ALL VALUES OF Q DIVIDED BY TWO

PRD

Range	T <sub>max</sub>	Q		HALF-Q		A <sub>max</sub> (Q) / A <sub>max</sub> (Half-Q)
		A <sub>max</sub>	T <sub>max</sub>	A <sub>max</sub>	T <sub>max</sub>	
5.63	0.9	1.0 x 10 <sup>5</sup>		0.9	3.0 x 10 <sup>4</sup>	3.3
16.1	2.5	1.8 x 10 <sup>4</sup>		2.5	7.2 x 10 <sup>3</sup>	2.5
56.3	2.8	1.4 x 10 <sup>3</sup>		3.2	3.5 x 10 <sup>2</sup>	4.0
161.0	5.6	2.1 x 10 <sup>2</sup>		5.6	1.1 x 10 <sup>2</sup>	1.9
563.0	10.0	4.1 x 10 <sup>1</sup>		10.0	3.1 x 10 <sup>1</sup>	1.3

PSRV

5.63	0.9	7.2 x 10 <sup>5</sup>		0.9	2.1 x 10 <sup>5</sup>	3.4
16.1	2.2	4.6 x 10 <sup>4</sup>		2.5	1.8 x 10 <sup>4</sup>	3.3
56.3	2.8	3.0 x 10 <sup>3</sup>		3.2	7.0 x 10 <sup>2</sup>	4.3
161.0	4.5	2.5 x 10 <sup>2</sup>		5.6	1.3 x 10 <sup>2</sup>	1.9
563.0	8.9	2.8 x 10 <sup>1</sup>		8.9	1.9 x 10 <sup>1</sup>	1.5

PSAA

5.63	0.7	5.1 x 10 <sup>6</sup>		0.9	1.5 x 10 <sup>6</sup>	3.4
16.1	0.7	2.5 x 10 <sup>5</sup>		2.5	4.5 x 10 <sup>4</sup>	5.6
56.3	2.8	6.7 x 10 <sup>3</sup>		3.2	1.4 x 10 <sup>3</sup>	4.8
161.0	3.6	3.7 x 10 <sup>2</sup>		5.6	1.4 x 10 <sup>2</sup>	2.6
563.0	7.1	2.3 x 10 <sup>1</sup>		8.9	1.4 x 10 <sup>1</sup>	1.6

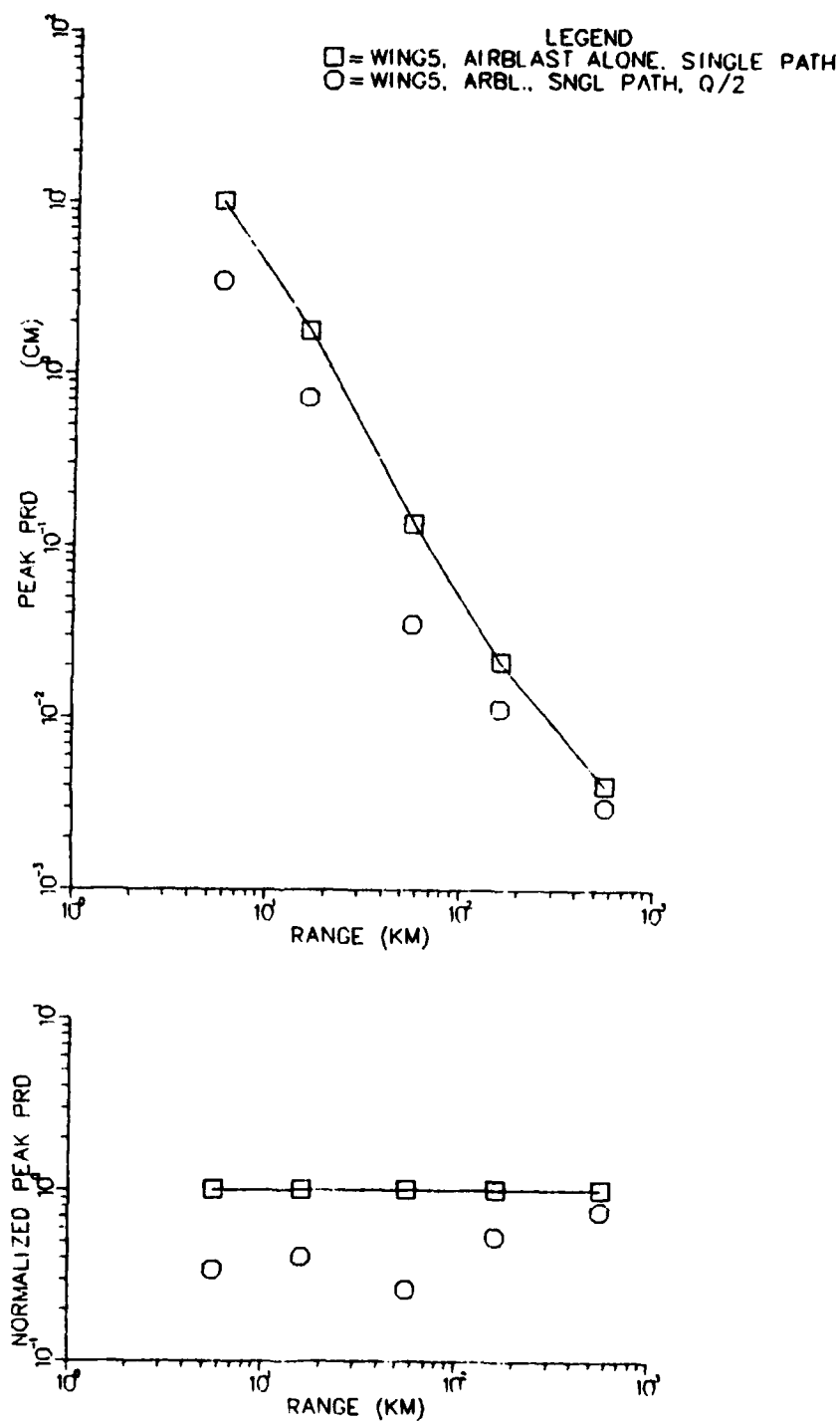


Figure 2la. Peak values of PRD are plotted for W5S3 using the Q model in Figure 5 and using that model with all values of Q divided by two.

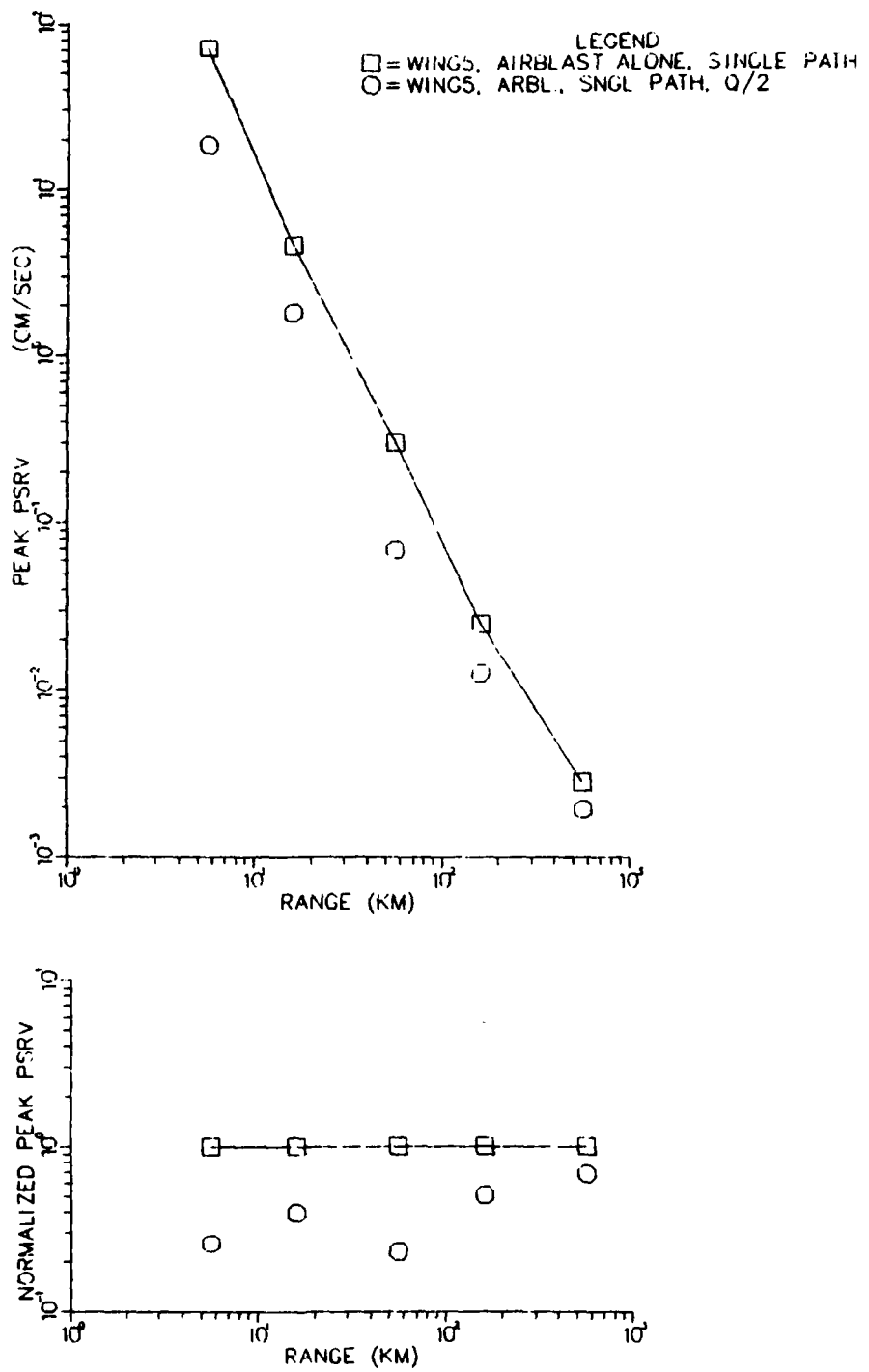


Figure 2lb. Peak values of PSRV are plotted for W5S3 using the Q model in Figure 5 and using that model with all values of Q divided by two.

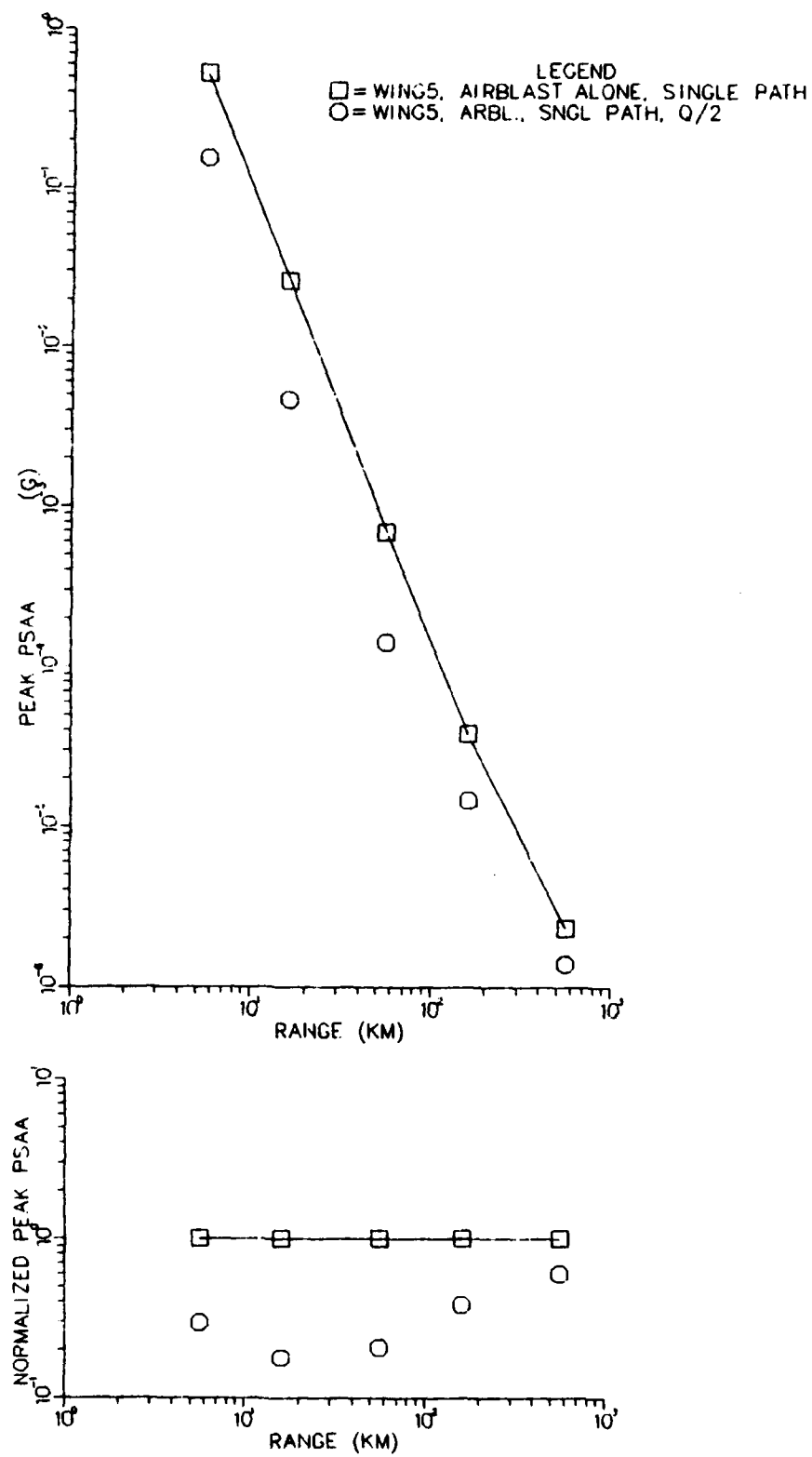


Figure 2lc. Peak values of PSAA are plotted for W5S3 using the Q model in Figure 5 and using that model with all values of Q divided by two.

## V. REFERENCES

- Alewine, R. W. (1974), "Application of Linear Inversion Theory Towards the Estimation of Seismic Source Parameters," Ph.D. Thesis, California Institute of Technology.
- Bache, T. C., T. G. Barker, N. Rimer and J. T. Cherry (1980), "The Contribution of Two-Dimensional Source Effects to the Far-Field Seismic Signatures of Underground Nuclear Explosions," Systems, Science and Software Topical Report submitted to the Advanced Research Projects Agency, SSS-R-80-4569, July.
- Bache, T. C., J. M. Masso and B. F. Mason (1977), "Theoretical Body and Surface Wave Magnitudes for Twelve Numerically Simulated Cratering Explosions," Systems, Science and Software Report submitted to the Advanced Research Projects Agency, SSS-R-77-3119, January.
- Bache, T. C., W. L. Rodi and D. G. Harkrider (1978), "Crustal Structures Inferred from Rayleigh Wave Signatures of NTS Explosions," BSSA, 68, pp. 1399-1413.
- Bache, T. C., H. J. Swanger and B. Shkoller (1980), "Synthesis of  $Lg$ ," Systems, Science and Software Report submitted to the Air Force Office of Scientific Research, SSS-R-81-4668, September.
- Burridge, R. and L. Knopoff (1964), "Body Force Equivalent for Seismic Dislocation," BSSA, 54, pp. 1875-1888.
- Cherry, J. T., T. C. Bache and D. B. Patch (1975), "The Teleseismic Ground Motion Generated by an Explosion in a Tunnel and Its Effect on the  $M_s/m_b$  Discriminant," Systems, Science and Software Final Report submitted to the Defense Nuclear Agency, DNA 3645F, May.
- Cherry, J. T., T. C. Bache, W. O. Wray and J. F. Masso (1976), "Teleseismic Coupling from the Simultaneous Detonation of an Array of Nuclear Explosions," Systems, Science and Software Technical Report submitted to the Advanced Research Projects Agency, SSS-R-76-2865, February.
- Green, A. G., O. G. Stephenson, G. D. Mann, E. R. Kanasewich, G. L. Cumming, Z. Hajnal, J. A. Mair and G. F. West (1980), Canadian Journal of Earth Sciences, 17(5).

V. REFERENCES (continued)

- Harkrider, D. G. (1964), "Surface Waves in Multilayered Media I. Rayleigh and Love Waves from Buried Sources in a Multilayered Elastic Halfspace," BSSA, 54, pp. 627-679.
- Harkrider, D. G. (1970), "Surface Waves in Multilayered Media II. Higher Mode Spectra and Spectral Ratios from Point Sources in Plane-Layered Earth Models," BSSA, 60, pp. 1937-1987.
- Healy, J. and D. Warren (1969), "Explosion Seismic Studies in North America in the Earth's Crust and Upper Mantle," Geophys. Monogr. Ser., 13, edited by P. Hart, pp. 208-220, American Geophysical Union, Washington, D. C.
- Herrmann, R. B. (1977), "Research Study of Earthquake Generated SH Waves in the Near-Field and Near-Regional Field," Final Report, Contract DACW39-76-C-0058, Waterways Experimental Station, Vicksburg, Mississippi.
- Keller, G. R., R. B. Smith, L. W. Braile, R. Heaney and D. H. Shurbert (1976), "Upper Crustal Structure of the Eastern Basin and Range, Northern Colorado Plateau and Middle Rocky Mountains from Rayleigh-Wave Dispersion," BSSA, 66, pp. 869-876.
- Murphy, J. R. and T. J. Bennett (1980), "Analysis of the Low Frequency Ground Motion Environment for MX: Surface Waves and Valley Reverberation," Systems, Science and Software Final Report submitted to the Defense Nuclear Agency, SSS-R-80-4298, January.
- Needham, C. C., M. L. Havens and C. S. Knauth (1975), "Nuclear Blast Standard (1 KT)," Air Force Weapons Laboratory Final Report AFWL-TR-73-55.
- Rimer, N., E. J. Halda and J. T. Cherry (1980), "Nonlinear Ground Motion from a Megaton Near Surface Nuclear Explosion," Systems, Science and Software Report submitted to the Air Force Geophysics Laboratory, AFGL-TR-80-0167, March.
- Sandler, I. (1978), "Outrunning Ground Motion Calculations," Minutes of the 15th Meeting of the Data Analysis Working Group, La Jolla, California.
- Swanger, H. J. and D. M. Boore (1978), "Simulation of Strong Motion Displacements Using Surface-Wave Modal Superposition," BSSA, 68(4), pp. 907-922.

## APPENDIX A

### SYNTHETIC SEISMOGRAMS FROM COMPLEX SOURCE CALCULATIONS

#### A.1 INTRODUCTION

There is increasing interest in the use of large scale finite difference or finite element computer programs to simulate the complex nonlinear material behavior that occurs in the region immediately surrounding earthquake or explosion sources. To fully appreciate the significance of the output of these programs, it is important to be able to compute the ground motions at ranges much larger than the maximum dimension of the computational grid. As long as the material response can be assumed to be linearly elastic outside the immediate source region, analytical techniques can be used to continue the wave field to the ranges of interest. In this Appendix we describe these techniques.

When the source is assumed to be embedded in an elastic wholespace, an "equivalent elastic source" representation can be constructed by expanding the outgoing wave field in spherical harmonics (e.g., Bache and Harkrider, 1976). The source is then expressed in terms of multipolar coefficients that can be used as input to programs for computing synthetic seismograms. This technique has been used to study the results from complex explosion (Cherry, et. al., 1975, 1976; Bache and Masso, 1978) and earthquake (Bache, et. al., 1980) sources computed with finite difference programs.

When boundaries (e.g., a free surface) are present in the vicinity of the source, the ground motions at

ranges outside the numerical grid can be computed with a wave field continuation method. Based on an elastodynamic representation theorem (e.g., Burridge and Knopoff, 1964). This method requires the convolution of stresses and displacements from the elastic region of the numerical source calculation with Green's functions representing the elastic wave propagation through the medium outside the source region.

In subsequent sections we begin with the formulation of the basic theory. For earthquake sources the wave field continuation must be done in three dimensions. However, many important complex explosion phenomena are axisymmetric and the theory is specialized for this case. Some of the development for the axisymmetric case can also be used for three-dimensional sources in plane-layered earth models, since the Green's functions are azimuth-independent for such structures.

The details of the implementation depend on the choice of Green's functions for the propagation. Our emphasis here is on the Rayleigh wave modes for plane-layered earth models. Test problems which illustrate this case and demonstrate the accuracy that can be achieved are presented, in Bache, et al. (1980).

#### A.2 FORMULATION

For the analytic continuation we use an elastodynamic representation theorem (Burridge and Knopoff, 1964). Assuming no body forces are present, this theorem may be written

$$u_i^F = - \int_{S_M} \left[ G_j^i * T_j^M - S_{jk}^i * u_j^M n_k \right] dA , \quad (A.1)$$

where the repeated indices imply summation and the following notation has been used:

$u^F(x_F, t)$ :	Components of the displacements at $x_F$ outside the source region;
$G_j^i(x_M, x_F, t)$ :	Displacement in the direction $j$ at $x_M$ due to a unit impulsive force at $x_F$ in the direction $i$ ;
$S_{jk}^i(x_M, x_F, t)$ :	The components of the stress tensor at $x_M$ due to a unit impulsive force at $x_F$ in direction $i$ ;
$T_j^M(x_M, t)$ :	Components of the monitored traction vector on the monitoring surface;
$u_j^M$ :	Components of the monitored displacement vector on the monitoring surface;
$n_k$ :	Components of the normal to the monitoring surface, with the positive sense being for vector pointing <u>away from the source</u> ;
$S_M$ :	Area of the monitoring surface.

Also, convolution is indicated by

$$f * g = \int_0^t f(t-\tau)g(\tau) d\tau . \quad (A.2)$$

Thus, the solution at some distant point is obtained by first convolving suitable Green's functions with stresses and displacements monitored on some surface that encloses the region of inelastic material deformation. The final solution is then obtained by integrating the convolution products over the monitoring surface. The restrictions on this technique are, first, that the region outside the monitoring surface must be linearly elastic. Second, if the problem domain is bounded, the Green's functions must satisfy appropriate boundary data. The elastic medium may be anisotropic or have discontinuous properties, though the computation of Green's functions is much more difficult for such media than for homogeneous isotropic media.

To this point the formulation is entirely general. Let us now consider cases where the source and propagation medium are axisymmetric. This is the appropriate geometry for explosions near the free surface (or other horizontal boundaries) in plane-layered earth models.

Stresses and displacements are monitored on some surface with a typical point M. We wish to compute the displacement field at F. Let the monitored quantities at M be denoted by  $\sigma_{rr}^M$ ,  $\sigma_{rz}^M$ ,  $\sigma_{zz}^M$ ,  $u_r^M$  and  $u_z^M$ . Then the components of the traction vector and displacement, referred to a local coordinate system  $(x_1, x_2, x_3)$  at F, are given by:

$$T_1^M = (\sigma_{rr}^M \cos\theta + \sigma_{rz}^M \sin\theta) \cos\xi ,$$

$$T_2^M = -(\sigma_{rr}^M \cos\theta + \sigma_{rz}^M \sin\theta) \sin\xi ,$$

$$T_3^M = \sigma_{rz}^M \cos\theta + \sigma_{zz}^M \sin\theta ,$$

$$u_1^M = u_r^M \cos \xi , \quad (A.3)$$

$$u_2^M = -u_r^M \sin \xi ,$$

$$u_3^M = u_z^M ,$$

$$n_1 = \cos \theta \cos \xi , n_2 = -\cos \theta \sin \xi , n_3 = \sin \theta .$$

Also, the displacements at F in the global R-z system are related to the displacements in the  $x_1, x_2, x_3$  system by

$$u_R^F = u_1^F \cos \psi - u_2^F \sin \psi , \quad (A.4)$$

$$u_z^F = u_3^F .$$

Using these coordinate transformations, (A.1) may be written:

$$\begin{aligned} u_R^F &= - \int_{S_M} r \left[ (G_r^R * \sigma_{rr}^M + G_z^R * \sigma_{rz}^M) - (S_{rr}^R * u_r^M + S_{rz}^R * u_z^M) \right] dz \\ &\quad - \int_{S_M} r \left[ (G_z^R * \sigma_{zz}^M + G_r^R * \sigma_{rz}^M) - (S_{rz}^R * u_r^M + S_{zz}^R * u_z^M) \right] dr , \\ u_z^F &= - \int r \left[ (G_r^Z * \sigma_{rr}^M + G_z^Z * \sigma_{rz}^M) - (S_{rr}^Z * u_r^M + S_{rz}^Z * u_z^M) \right] dz \\ &\quad - \int r \left[ (G_z^Z * \sigma_{zz}^M + G_r^Z * \sigma_{rz}^M) - (S_{rz}^Z * u_r^M + u_r^M + S_{zz}^Z * u_z^M) \right] dr , \end{aligned}$$

where the quantities  $G_r^R, G_z^R$ , etc., are azimuthal averages of the Green's functions in the  $x_1, x_2, x_3$  system. The explicit formulas for the azimuthally averaged Green's functions are the following:

$$G_r^R = \int_0^{2\pi} [G_1^1 \cos \psi \cos \xi - G_2^1 \sin (\xi + \psi) + G_2^2 \sin \xi \sin \psi] d\phi$$

$$G_z^R = \int_0^{2\pi} [G_3^1 \cos \psi - G_3^2 \sin \psi] d\phi, \quad (A.6)$$

$$G_r^Z = \int_0^{2\pi} [G_1^3 \cos - G_2^3 \sin] d\phi,$$

$$G_z^Z = \int_0^{2\pi} [G_3^3] d\phi, \quad (A.7)$$

where  $G^1(x_M, x_F, t)$ , etc., are evaluated at  $x_{2F} = 0$ . Also,  $x_M = (x_1, x_2, x_3)$ , with

$$x_1^2 = R_F^2 + r_M^2 - 2r_M R_F \cos \phi,$$

$$x_2 = 0,$$

$$x_3 = z_M - z_F. \quad (A.8)$$

For axisymmetric problems formulated to compute the solution in the  $\omega$ ,  $k$  domain (e.g., modal solutions), the azimuthal integrations in (A.6) and (A.7) may be computed analytically. In the  $p$ ,  $t$  domain (e.g., generalized ray theory), these integrations cannot, in general, be performed analytically. However, in the far-field, an analytic approximation for these integrals may be used.

The formulas for the azimuthally averaged stress Green's functions,  $S_{rr}^R$ , etc., are given by:

$$S_{rr}^R = \int_0^{2\pi} \left[ \begin{array}{l} (S_{11}^1 \cos^2 \xi - S_{21}^1 \sin 2\xi + S_{22}^1 \sin^2 \xi \cos \psi) \\ - (S_{11}^2 \cos^2 \xi - S_{21}^2 \sin 2\xi + S_{22}^2 \sin^2 \xi) \sin \psi \end{array} \right] d\phi,$$

$$s_{zr}^R = \int_0^{2\pi} \left[ (s_{31}^1 \cos\xi - s_{32}^1 \sin\xi) \cos\psi - (s_{31}^2 \cos\xi - s_{32}^2 \sin\xi) \sin\psi \right] d\phi \quad (A.9)$$

$$s_{rr}^z = \int_0^{2\pi} \left[ s_{11}^3 \cos^2\xi - s_{21}^3 \sin 2\xi + s_{22}^3 \sin^2\xi \right] d\phi ,$$

$$s_{zr}^R = \int_0^{2\pi} \left[ s_{31}^1 \cos\xi - s_{32}^2 \sin\xi \right] d\phi ,$$

$$s_{zz}^z = \int_0^{2\pi} \left[ s_{33}^1 \cos\psi - s_{33}^2 \sin\psi \right] d\phi$$

$$s_{zz}^z = \int_0^{2\pi} s_{33}^3 d\phi .$$

If the azimuthal averages in (A.6) and (A.7) can be analytically determined, it is not necessary to use (A.9). Instead, the constitutive equation of the medium at the monitoring point can be used. Thus, for an isotropic medium

$$\begin{aligned} s_{rr}^z &= \lambda \left( \frac{\partial G_r^z}{\partial r} + \frac{G_r^z}{r} + \frac{\partial G_z^z}{\partial z} \right) + 2\mu \frac{\partial G_r^z}{\partial r} , \\ s_{zz}^z &= \lambda \left( \frac{\partial G_r^z}{\partial r} + \frac{G_r^z}{r} + \frac{\partial G_z^z}{\partial z} \right) + 2\mu \frac{\partial G_z^z}{\partial z} , \\ s_{rz}^z &= \mu \left( \frac{\partial G_r^z}{\partial z} + \frac{\partial G_z^z}{\partial r} \right) , \end{aligned} \quad (A.10)$$

where  $\lambda$  and  $\mu$  are Lame's constants, and formulas of the same type can be written for  $S_{rr}^R$ ,  $S_{rz}^R$  and  $S_{zz}^R$ .

The basic formulation for analytical continuation of axisymmetric source computations is now complete. These equations are valid for a monitoring surface of arbitrary shape. Implementation requires the computation of Green's functions appropriate for the application of interest.

### A.3 FORMULATION FOR SURFACE WAVES

For many problems the primary interest is in the normal mode contribution to the solution for waves in layered media. For such problems the analysis is more conveniently done in the frequency - wave number domain.

We will develop the solution using Green's functions computed following Harkrider (1964, 1970), though the theory is easily modified to use alternative techniques for computing Rayleigh wave modes.

For the azimuthally averaged Rayleigh wave displacement, Green's functions for a particular mode are:

$$\begin{aligned} G_r^R &= i\pi A_R \epsilon_0 X(z) J_1(kr) H_1^{(2)}(kr), \\ G_z^R &= i\pi A_R \epsilon_0 W(z) J_0(kr) H_1^{(2)}(kr), \\ G_z^Z &= \pi A_R X(z) J_1(kr) H_0^{(2)}(kr), \\ G_z^Z &= \pi A_R W(z) J_0(kr) H_0^{(2)}(kr), \end{aligned} \quad (A.11)$$

where  $X(z)$  and  $W(z)$  are the normalized horizontal and vertical displacement eigenfunctions and  $\epsilon_0$  is the ellipticity. The  $A_R$  is the amplitude response,  $k$  is wave

number,  $r$  is the radial distance to a point on the monitoring surface and  $R$  is the range.

The stress Green's functions are easily computed from (A.10) using the following identities given by Harkrider (1970):

$$\frac{\partial X(z)}{\partial z} = k \left( W(z) + \frac{\tau(z)}{\mu} \right) , \quad (A.12)$$

$$\frac{\partial W(z)}{\partial z} = -k \left( \frac{\lambda X(z) + \Sigma(z)}{\lambda + 2\mu} \right) ,$$

where  $\tau(z)$  and  $\Sigma(z)$  are the normalized horizontal and vertical stress eigenfunctions.

Anelastic attenuation is incorporated using the standard  $e^{-Y(\omega)r}$  operator. The parameter  $Y$  is computed from specified values of  $Q$  for each layer in the crustal model.

DAT  
ILM